JOURNAL OF GEOPHYSICAL RESEARCH, VOL. 112, B07303, doi:10.1029/2006JB004672, 2007

Upper mantle structure beneath the Galápagos Archipelago from surface wave tomography

Darwin R. Villagómez,[1] Douglas R. Toomey,[1] Emilie E. E. Hooft,[1] and Sean C. Solomon[2]

Received 31 July 2006; revised 2 February 2007; accepted 7 March 2007; published 4 July 2007.

[1] We present a Rayleigh wave tomographic study of the upper mantle beneath the Galápagos Archipelago. We analyze waves in 12 separate frequency bands (8–50 mHz) sensitive to shear wave velocity (V_S) structure in the upper 150 km. Average phase velocities are up to 2 and 8% lower than for 0- to 4-My-old and 4- to 20-My-old Pacific seafloor, respectively. Laterally averaged V_S is 0.05–0.2 km/s lower between 75- and 150-km depth than for normal Pacific mantle of comparable age, corresponding to an excess temperature of 30 to 150°C and ~0.5% melt. A continuous low-velocity volume that tilts in a northerly direction as it shoals extends from the bottom of our model to the base of a high-velocity lid, which is located at depths varying from 40 to 70 km. We interpret this low-velocity volume as an upwelling thermal plume that flattens against the base of the high-velocity lid. The high-velocity lid is ~30 km thicker than estimated lithospheric thickness beneath the southwestern archipelago, above the main region of plume upwelling. We attribute the thicker-than-normal high-velocity lid to residuum from hot spot melting. The thickness of the lid appears to control the final depth of melting and the variability of basalt composition in the archipelago. At depths less than 100–120 km, plume material spreads in directions both toward and against eastward plate motion, indicating that plume buoyancy forces dominate over plate drag forces and suggesting a relatively high plume buoyancy flux ($B \geq 2000$ kg/s).

Citation: Villagómez, D. R., D. R. Toomey, E. E. E. Hooft, and S. C. Solomon (2007), Upper mantle structure beneath the Galápagos Archipelago from surface wave tomography, *J. Geophys. Res.*, *112*, B07303, doi:10.1029/2006JB004672.

1. Introduction

[2] Hot spot volcanism is widely thought to be the result of upwelling and melting of hot, buoyant mantle [*Morgan*, 1971]. Gravity and topography observations of hot spot swells and results from modeling suggest that these mantle upwellings or plumes rise to the base of the lithosphere where they spread laterally [e.g., *Ribe and Christensen*, 1994; *Feighner and Richards*, 1995; *Sleep*, 1996]. Some plumes interact with nearby spreading centers and produce physical and chemical anomalies along some 15–20% of the global mid-ocean ridge system, although the precise mechanism and depth of transport of plume material to mid-ocean ridges are still matters of debate [*Ito et al.*, 2003, and references therein]. Lubrication theory and models predict that for off-axis plumes the main factors that control plume-ridge interaction are gravitational spreading of a plume layer that pancakes beneath the sloping base of the lithosphere and drag by the overriding plate [*Ribe*, 1996; *Ito et al.*, 1997; *Ribe and Delattre*, 1998]. Alternatively, for a sufficiently low-viscosity asthenosphere plume flow could also be driven by pressure gradients associated with plate creation at ridges [*Yale and Phipps Morgan*, 1998; *Toomey et al.*, 2002b].

[3] Although regional seismic tomography has provided compelling evidence for plume-like upwelling in the upper mantle [e.g., *Granet et al.*, 1995; *Wolfe et al.*, 1997; *Ritter et al.*, 2001; *Allen et al.*, 2002; *Li and Detrick*, 2006], the resolution of images of off-axis hot spots in the uppermost mantle has not been adequate to provide clear tests of models of plume spreading and plume-ridge interaction. To address these issues we present a surface wave tomographic study of the Galápagos Archipelago. The main goal of our study is to characterize the upwelling, spreading, and melting of the shallow mantle beneath the Galápagos hot spot. The Galápagos Archipelago is an excellent setting to study the dynamics of the interaction among hot spots, the lithosphere, and a mid-ocean ridge, because of the proximity of the hot spot to the Galápagos Spreading Center (GSC) and because the direction of plate drag over the hot spot (eastward) is approximately perpendicular to the relative spreading direction of the GSC (north-south).

2. Regional Setting

[4] The Galápagos hot spot, located in the equatorial east Pacific, consists of 10 major volcanic islands and 21 emergent volcanoes (Figure 1). The islands sit on a shallow and broad submarine platform (the Galápagos swell) that is

[1]Department of Geological Sciences, University of Oregon, Eugene, Oregon, USA.
[2]Department of Terrestrial Magnetism, Carnegie Institution of Washington, Washington, District of Columbia, USA.

0148-0227/07/2006JB004672$09.00

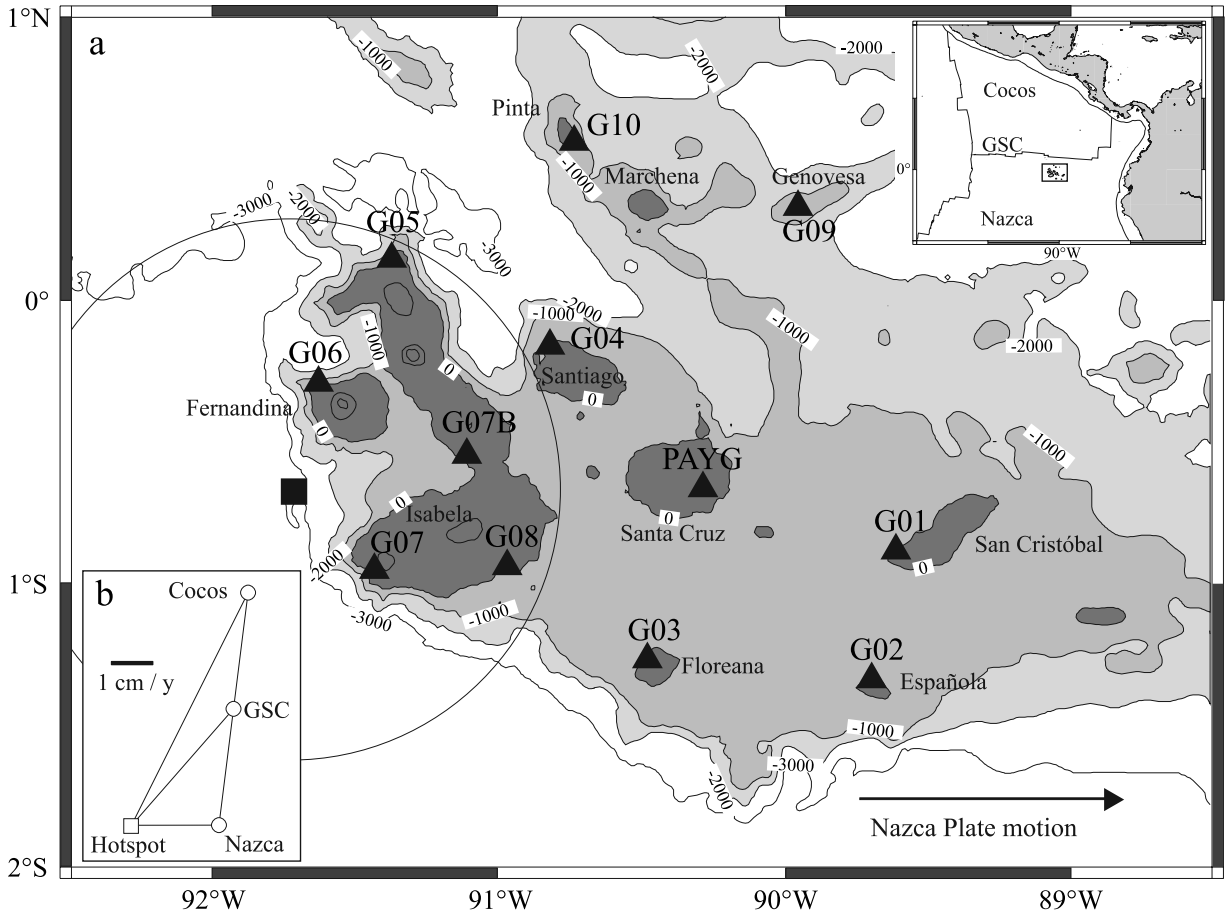

Figure 1. (a) Map of the Galápagos Islands and seismic network. Triangles indicate seismic stations. The black square and solid circle with a 100-km radius indicate the approximate center and area of a region of anomalously thin mantle transition zone [*Hooft et al.*, 2003]. The black arrow indicates the direction of motion of the Nazca plate in a hotspot reference frame [*Gripp and Gordon*, 2002]. Bathymetry is from W. Chadwick (http://newport.pmel.noaa.gov/~chadwick/galapagos.html) 1000-m contour interval. (b) Vector velocities of plates and other features in the Galápagos region.

elevated more than 2000 m above the surrounding ocean floor. An oceanic fracture zone crosses the northern part of the Galápagos near 91°W and creates a ~5-My lithospheric age offset, with thinner lithosphere beneath the eastern part of the archipelago. The hot spot sits on the Nazca plate, which moves eastward with respect to the hot spot, in a direction approximately perpendicular to the north-south (N-S) spreading of the GSC.

[5] Evidence of a plume origin for the Galápagos hot spot includes basalts enriched in incompatible elements (for example, higher $^{3}He/^{4}He$ and $^{87}Sr/^{86}Sr$ and lower $^{143}Nd/^{144}Nd$) [*White and Hofmann*, 1978; *Geist et al.*, 1988; *White et al.*, 1993; *Kurz and Geist*, 1999; *Harpp and White*, 2001], a general progression of the age of volcanism away from the hot spot in the direction of plate motion [*McBirney and Williams*, 1969; *Sinton et al.*, 1996], and seismic images of anomalous upper mantle structure. *Hooft et al.* [2003] used receiver functions to show that the 410-km mantle discontinuity is deflected downward within an area approximately 100 km in radius centered beneath the southwestern corner of the archipelago (Figure 1). This anomaly reflects higher temperatures (130 ± 60 K) across that phase transition, consistent with upwelling from depths greater than 410 km [*Hooft et al.*, 2003]. Above the downward-deflected 410-km discontinuity, body wave tomography resolves low seismic velocities at depths of 50–250 km, consistent with upwelling of anomalously hot mantle [*Toomey et al.*, 2002a].

[6] Several unique features make the Galápagos Archipelago different from more conventional hot spots such as Hawaii. First, while volcanism shows a general age progression in the direction of plate motion, the progression is not monotonic; almost all of the Galápagos Islands have erupted in the Holocene [*Simkin and Siebert*, 1994]. Second, geochemical signatures of basalts show an unusual spatial distribution: depleted basalts appear near the center and northeastern part of archipelago, while enriched lavas appear primarily along the western and southern parts [*White and Hofmann*, 1978; *Geist et al.*, 1988; *White et al.*, 1993; *Kurz and Geist*, 1999; *Harpp and White*, 2001]. Moreover, the Galápagos hot spot influences magmatism and tectonics on the GSC, an inference evident in correlated variations in geophysical, geochemical, and volcanological manifestations along the ridge [*Detrick et al.*, 2002]. These variations along the GSC axis are more or less symmetric about 91.5°W [*Schilling et al.*, 2003].

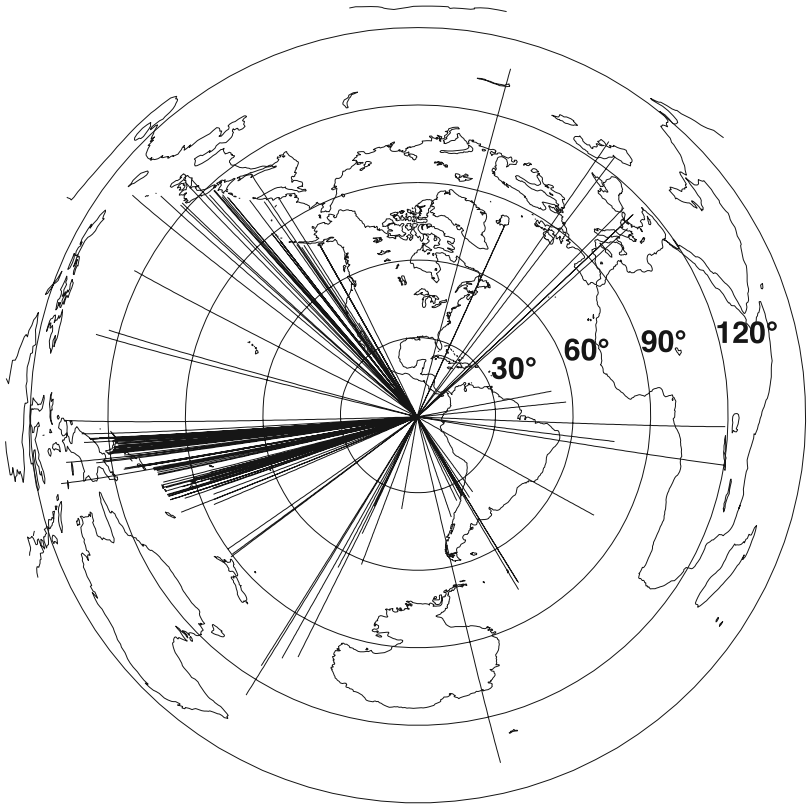

Figure 2. Azimuthal distribution of the 189 events ($M_S > 5.9$) for which Rayleigh waves were analyzed in this study. Epicentral distance varies from 40° to 140°. Solid lines correspond to great circle paths. Azimuthal equidistant projection centered at 0°N, 90°W.

[7] Two general models of mantle upwelling for the Galápagos hot spot have been proposed. The first model is based on geochemical data from the archipelago and accounts for the Nazca plate moving eastward with respect to the hot spot. *Richards and Griffiths* [1989] and *White et al.* [1993] suggested that the particular spatial distribution of incompatible elements in the archipelago could be the result of thermal entrainment of depleted upper mantle, as a result of local convective overturn within the center of a deflected mantle upwelling or plume. In this view, the plume is deflected to the east in the shallow mantle in response to plate drag. However, this model does not take into account the observed geochemical and geophysical variations along the axis of the GSC. The second model is based on geodynamical modeling of hot spot-ridge interaction and accounts for the effect of N-S seafloor spreading [*Ito et al.*, 1997]. The model includes northward migration of the GSC relative to the hot spot but does not account for eastward Nazca plate motion. Hot spot-derived material is transported to the ridge symmetrically to the east and west, accounting for the symmetrical along-axis geochemical variations, but the model does not consider the asymmetrical geochemical patterns observed within the archipelago. To date, no model can account for all of the geophysical and geochemical observations at both the GSC and the Galápagos Archipelago.

[8] To study the upper mantle beneath the Galápagos and test models of plume-ridge-lithosphere interaction we conducted a broadband seismic experiment. Seismic stations were deployed on nine islands of the archipelago between September 1999 and March 2003 (Figure 1). The network consisted of 10 portable broadband stations and the Global Seismographic Network station PAYG. The station spacing was between 50 and 70 km. Three-component Streckeisen STS-2 sensors were used at all portable stations; two Guralp CMG-3ESP instruments were initially deployed but were replaced after the first year. Data loggers were PASSCAL-equivalent Reftek units recording continuously at 20 samples per second. The seismic network spanned an area approximately 200 km in diameter. For this study we use three-component recordings of Rayleigh waves generated by 186 teleseismic events with $M_S > 5.9$ at epicentral distances ranging between 40° and 140° (Figure 2).

3. Method

3.1. Imaging of Phase Velocity

[10] The seismic data are first used to derive one- and two-dimensional images of Rayleigh wave phase velocity. We obtain phase and amplitude information from the vertical-component seismograms. After correcting for instrument response, the data are windowed and filtered into 12 different frequency bands using a 10-mHz-wide, fourth-order, zero-phase Butterworth filter. The center frequencies are between 8 and 50 mHz, or 20- to 125-s period (Figure 3), corresponding to seismic wavelengths of ~80–500 km. Fundamental Rayleigh waves are sensitive to structure to a depth of approximately one wavelength, with peak sensi-

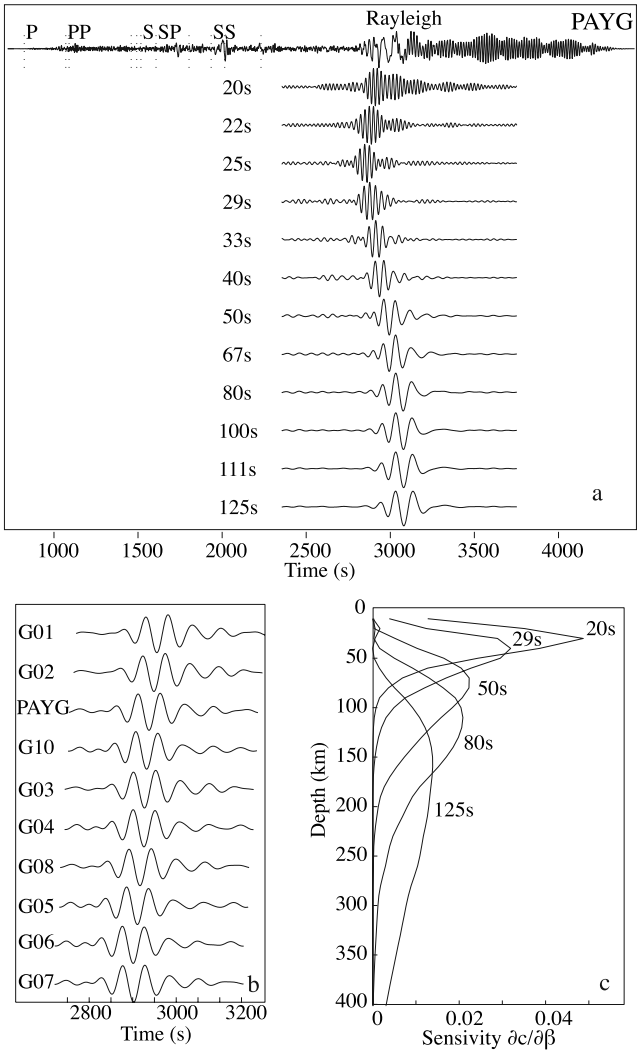

Figure 3. (a) Vertical seismograms for station PAYG for an event that occurred in the Vanuatu Islands on 26 November 1999 (M_S 7.3, epicentral distance 100°, back azimuth 253°). Unfiltered seismogram on top and bandpass-filtered Rayleigh waves for periods 20 to 125 s below. (b) Rayleigh waves filtered at 50-s period, on vertical seismograms for all recording stations. (c) Sensitivity kernels for Rayleigh waves as functions of depth for periods of 20, 29, 50, 80, and 125 s.

tivity in depth at about 1/3 of the wavelength (Figure 3c). We measure the amplitude and phase of each bandpassed-filtered seismogram using the discrete Fourier transform. To ensure data quality we select Rayleigh waves having amplitudes at least 2.5 times greater than that of the preceding body waves. Furthermore, we use seismograms only from events for which the waveforms from station to station are similar, i.e., for which the average normalized cross-correlation coefficient is greater than 0.9.

[11] Propagation effects outside the network, as well as heterogeneous structure within the network, can affect Rayleigh waves. In order to account for wave-propagation effects outside the network, such as multipathing, we use a two-plane wave approximation technique [*Forsyth and Li*, 2005]. At each frequency ω, the incoming wavefield of a particular event is represented as the sum of two plane waves of the form

$$U_z(\omega) = A_1(\omega)\exp[-i(\mathbf{k_1}\bullet\mathbf{x}-\omega t)] + A_2(\omega)\exp[-i(\mathbf{k}_2\bullet\mathbf{x}-\omega t)], \quad (1)$$

where U_z is vertical displacement, A_i is the amplitude of each incoming plane wave, $\mathbf{k_i}$ is the horizontal wave number vector, $\mathbf{x}$ is the position vector, and t is time. *Li et al.* [2003] showed that when this method was used in Rayleigh wave tomography in eastern North America it provided 30–40% variance reduction compared with the standard one-plane wave method.

[12] To characterize the heterogeneous structure within the network, the target volume is parameterized using a grid of nodes. The phase velocity is defined at each of these nodes by

$$V(\omega,\theta) = B_0(\omega) + B_1(\omega)\cos(2\theta) + B_2(\omega)\sin(2\theta), \quad (2)$$

where B_0 is the azimuthally averaged phase velocity, B_i are the anisotropic phase velocity coefficients, θ is the azimuth of propagation, and ω is frequency. We assume that higher-order azimuthal terms (4θ terms) are small for Rayleigh waves [*Smith and Dahlen*, 1973]. The direction of fast propagation is $\frac{1}{2}$ arctan (B_2 / B_1), and the peak-to-peak amplitude or degree of anisotropy is $2(B_1^2 + B_2^2)^{1/2}$ / B_0. We invert the frequency-dependent phase and amplitude data separately for each period band.

[13] Because of their finite frequency, surface waves are sensitive to two-dimensional structure near the propagation path. To account for these effects we calculate two-dimensional sensitivity kernels for fundamental Rayleigh waves by means of a single-scattering (Born) approximation [*Zhou et al.*, 2004; *Yang and Forsyth*, 2006]. For each frequency band, the phase and amplitude sensitivity kernels are calculated for phase velocity perturbations and are incorporated into the isotropic phase velocity inversions (Figure 4).

[14] The solution of the nonlinear inverse problem for plane wave and phase velocity parameters is performed as a two-stage iteration process [*Forsyth and Li*, 2005]. In the first stage of each iteration, velocity is held fixed and the best fitting parameters for the two-wave approximation are found for each using the downhill simplex method of simulated annealing [*Press et al.*, 1992]. In the second stage, corrections to the velocity model and wave parameters are determined using the linearized inversion technique of *Tarantola and Valette* [1982]. The observed data, the real and imaginary components at a single frequency, are initially assigned equal variance. Experience shows that a typical misfit to the normalized real and imaginary terms is on the order of 0.1, which we choose as an initial a priori estimate of standard deviation.

[15] We also assume that the solution (velocity parameters) is not too far from an initial estimate, so we penalize changes from this starting model. This penalty is achieved by introducing nonzero terms in the diagonals of the a priori model covariance matrix. The amount of penalization is controlled by the parameter σ_o, which is the a priori value of the standard deviation for the velocity terms in the inversion. This parameter is an estimation of the allowed varia-

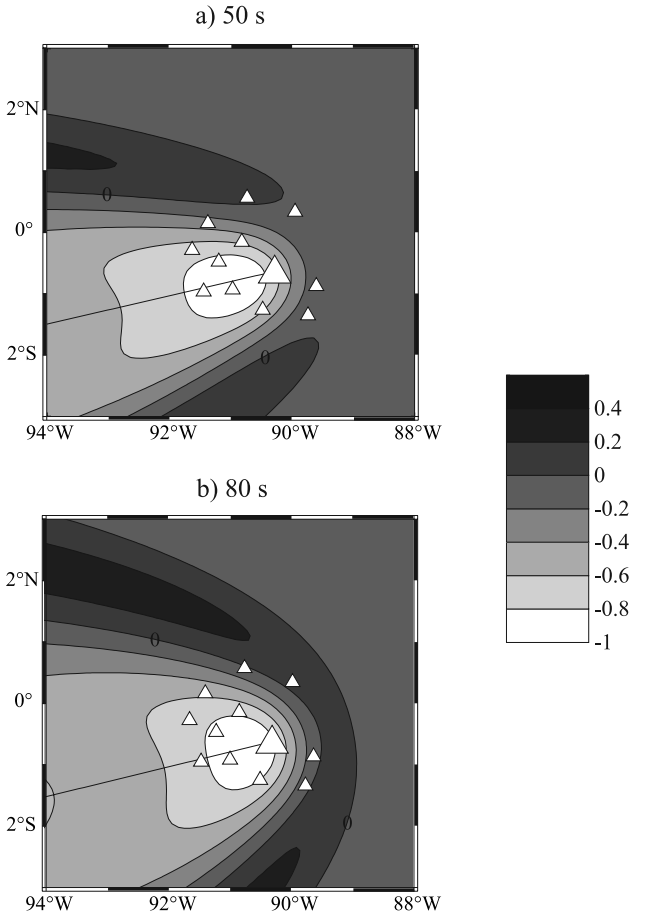

Figure 4. Normalized two-dimensional phase sensitivity kernels to local phase velocity perturbation showing the first negative and positive sensitivity regions for the event depicted in Figure 3 and station PAYG at (a) 50-s period and (b) 80-s period. White triangles represent seismic stations, the larger triangle denotes station PAYG, and the black line indicates the great circle path.

tions with respect to the starting model. In addition, we position a set of nodes surrounding the region of interest, for which we allow more variation; this outer ring of nodes absorbs additional traveltime variations not accounted for by structure inside the target volume.

[16] To remove the influence of events that are not well described by the two-plane wave approximation, each inversion is performed in two sets of iterations. In the first set, all the observations are assigned equal variance or weight, as expressed above. Then, in the second set of iterations, the observations are assigned variances based on the resulting standard deviations found after the first set of iterations. This sequence ensures that poor wavefield models are given less weight and do not bias the inversion. To describe the quality of fit to the data we use the root-mean square (RMS) misfit of the phase in seconds, which represents the misfit that is most directly related to traveltimes and the velocity structure.

3.2. Inversion for V_s

[17] The estimates of isotropic phase velocity are in turn used to constrain the shear wave velocity (V_S) structure. Changes in the phase velocity of a Rayleigh wave are mainly sensitive to perturbations in shear wave velocity and less to perturbations in compressional wave velocity (V_P) or density. We perform inversions for one-dimensional V_S structure at each grid node by finding the best fit between the observed phase velocities and those predicted by the code DISPER80 [*Saito*, 1988], which calculates normal modes for laterally homogeneous media. This technique yields predicted isotropic phase velocities from a given shear wave velocity model, as well as sensitivity kernels for V_S, V_P, and density. These sensitivity kernels are used in the inversion for V_S perturbations from a starting model in an iterative process using the linearized inversion technique of *Tarantola and Valette* [1982]. The inversion results are values of V_S as a function of depth and estimates of standard deviation.

[18] Because the inversion for shear wave velocity is underdetermined we must assume some a priori information about the model parameters. We use an a priori model covariance matrix of the form [e.g., *Tarantola and Valette*, 1982]:

$$\mathrm{Cm}_{ij} = \sigma_i^2 \exp\left[-\left(D_i - D_j\right)^2 / \left(2\,\Delta^2\right)\right], \qquad (3)$$

where D is depth, Δ is the characteristic length of smoothing, and σ_i is the a priori estimate of the standard deviation of the ith velocity term in the inversion. We assume that the resulting shear wave velocities are not too far from an initial estimate, so we penalize changes from this starting model by introducing nonzero terms in the diagonals of Cm. The amount of penalization is controlled by the parameter σ_i. A lower value of σ_i represents a higher penalty and greater damping of the solution. Using different values of σ_i for different layers allows us to constrain selectively the different parts of the model. Additionally, we introduce the assumption that the resulting velocity model is smooth. We impose smoothness on the model for the ith parameter by penalizing differences in velocity with respect to neighboring points, through the introduction of non-zero terms to the off-diagonals of the a priori model covariance matrix weighted using the characteristic distance Δ.

[19] A three-dimensional V_S model is constructed by merging all the one-dimensional V_S results obtained at each node. This three-dimensional model is generally smoother in the vertical direction than laterally, and so we apply horizontal smoothing within each depth layer using a two-dimensional moving average of neighboring points. When smoothing laterally, we allow changes only up to a small fraction of the standard deviation, usually 10–20%. The resulting model is thus smooth in both the vertical and lateral directions, and in our experience the maximum magnitude of a typical velocity anomaly is somewhat decreased but its spatial extent is preserved.

4. Results

[20] We first present results concerning the validity of the two-plane wave approximation method and a comparison with estimates of the direction of propagation obtained independently from polarization analysis. Second, we show results of inversions for one- and two-dimensional phase velocity,

for cases with and without anisotropy. Third, we present images of three-dimensional V_S structure derived from the two-dimensional isotropic phase velocity inversions.

4.1. Validity of the Two-Plane-Wave Approximation

[21] Results of the two-plane wave approximation show that in general the primary wave is much larger in amplitude than the secondary wave. The average ratio of the primary wave amplitude to the secondary wave amplitude decreases with frequency from 7.9 at 8 mHz (125 s period) to 2.8 at 50 mHz (20 s period). This decrease is expected because higher frequency waves are more strongly affected by focusing and multipathing. Furthermore, deviations from great circle path are less than 30° for the primary waves.

[22] To test the validity of the two-plane wave approximation we compare the two-plane wave results with those obtained independently from polarization analysis [*Vidale*, 1986]. To ensure measurement quality we use the cutoff parameters of *Larson and Ekström* [2002] for Rayleigh waves. Measurements of the direction of propagation of Rayleigh waves using polarization analysis confirm that deviations from great circle paths are small (less than 30°). Moreover, polarization analysis and the two-plane wave approximation are generally in good agreement on the primary direction of propagation (Figure 5).

[23] To investigate if local topography affects the propagation of Rayleigh waves, we measure the scattering of the arrival angles for all events at each station from polarization analysis. If there is a local topographic effect, there should be noticeable scattering of the individual arrival angles. Moreover, if topographic effects are important, scattering should be frequency dependent, because higher-frequency waves are more sensitive to topography than lower-frequency waves. The amount of scattering is quantified using the standard deviation of the individual measurements. We found that the scattering of measurements is relatively small (averaging 8.4 ± 5.1° for all events), and that there is no frequency dependence at the 95% confidence level. We conclude that the effect of local topography on the propagation of Rayleigh waves is not significant and that the incoming wavefield can be accurately described by the two-plane wave approximation.

4.2. Phase Velocity Inversion

[24] We present results from four sets of inversions for frequency-dependent phase velocity. In all inversions we use a regular grid of nodes separated by 0.2° in latitude and longitude (Figure 6a); this grid is encompassed by a set of nodes with larger prior uncertainties. Figure 6b shows the typical path coverage used for the phase velocity inversions. Table 1 shows the number of events and observations and the resulting RMS phase misfits for all inversions.

[25] In the first set of inversions we solve for the isotropic component of phase velocity, B_0, which is kept constant at all grid nodes. These results provide a uniform isotropic phase velocity for the entire region for each period. We use an initial value of phase velocity of 3.8 km/s and $\sigma_o = 0.1$ as the a priori value of the standard deviation for the phase velocity.

[26] Results of the inversion show that phase velocity increases with period from 3.625 ± 0.005 to 4.05 ± 0.02 km/s for periods from 20 to 125 s (Figure 7). These values are

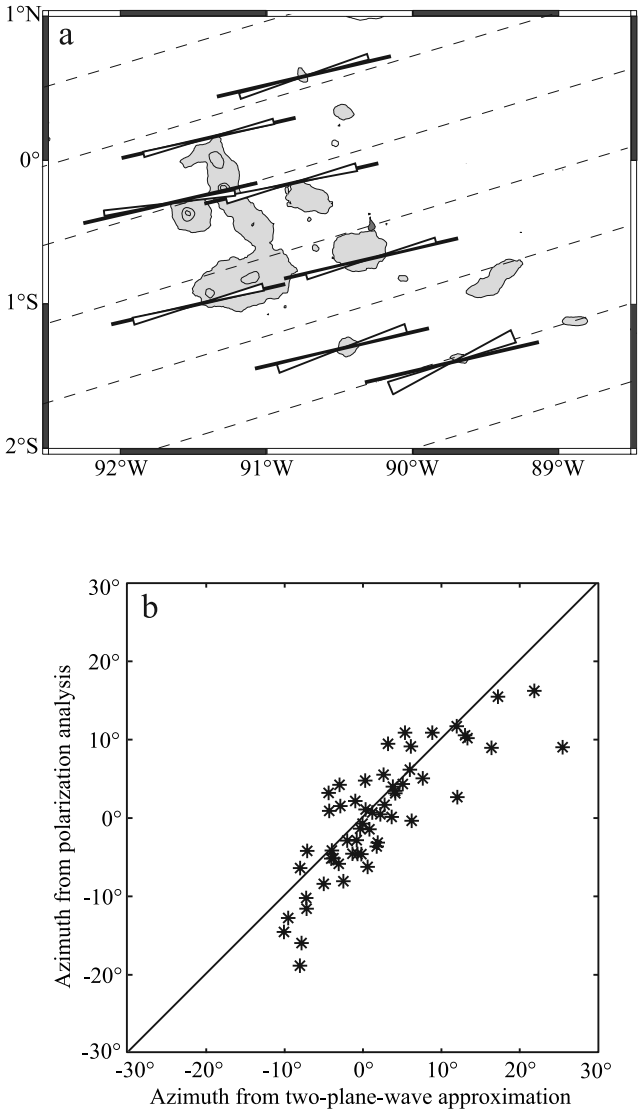

Figure 5. Results from the two-plane wave approximation and polarization analysis. (a) Polarization direction of Rayleigh waves for the event shown in Figure 3. Filled white bars indicate the direction from polarization analysis and its uncertainty. Dashed lines show great circle paths, and solid lines indicate the direction of the primary wave from the two-wave approximation. (b) Deviation from great circle path of the first plane wave from the two-wave approximation compared with the mean deviation from great circle path from polarization analysis for a 29-s period and events with an amplitude ratio of primary to secondary waves of greater than 4.

consistently lower than values for Pacific lithosphere of comparable age [*Nishimura and Forsyth*, 1989], although this difference is less pronounced at longer periods. At periods of 20 to 67 s the phase velocity is 2 to 2.5 % lower than for Pacific lithosphere 0–4 My old (0–4NF89) and 4.5 to 8% lower than for Pacific lithosphere 4–20 My old (4–20NF89). At longer periods, 80 to 125 s, phase velocities are 0 to 2% lower than for 0–4NF89 and 2.5 to 4% lower than for 4–20NF89. Phase velocities are 1–2% higher than values for Iceland [*Li and Detrick*, 2006], except at periods 25 to 50 s where they are

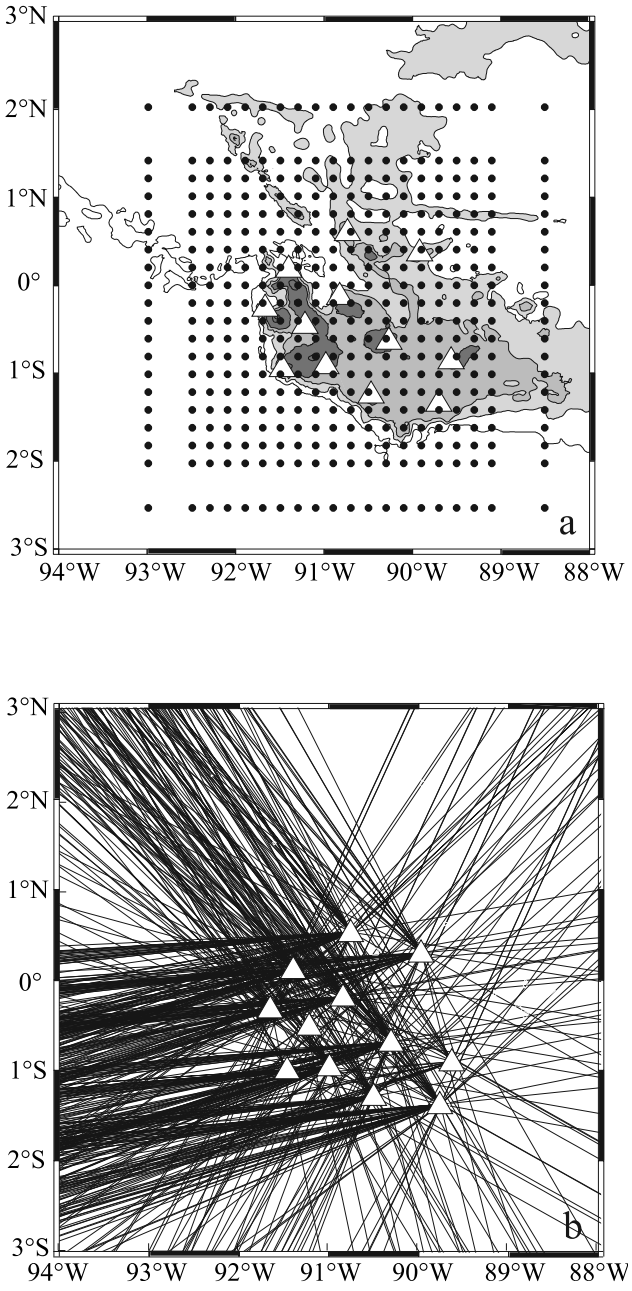

Figure 6. (a) Grid node parameterization used in the phase velocity inversions. (b) Path coverage for 50-s phase velocity inversion. White triangles denote seismic stations.

similar, and are comparable to young Pacific lithosphere near the East Pacific Rise (EPR) [*Forsyth et al.*, 1998] (Figure 7).

[27] In a second set of inversions, we add uniform azimuthal anisotropy and solve for the phase velocity parameters (B_0, B_1, and B_2), which are kept constant at all grid nodes. We use $\sigma_o = 0.1$ as an a priori value of standard deviation for the velocity and anisotropy terms. Results from the inversion show that the coefficient B_0 changes by less than 0.3% from the previous isotropic inversion. From the coefficients B_1 and B_2 we obtain average values of the fast direction of propagation and amplitude of 2θ anisotropy for the entire region. Measurements of seismic anisotropy provide an important constraint on mantle flow. Finite strain induces lattice-preferred orientation (LPO) of minerals, such as the alignment of the olivine *a* axis [e.g., *Christensen*, 1984]. Because olivine, the most abundant mineral in the upper mantle, is seismically anisotropic, the alignment of crystallographic *a* axes caused by mantle flow can produce measurable anisotropy.

[28] The peak-to-peak amplitude of azimuthal anisotropy varies between 0.2 and 1% (0.3–0.5% standard deviation) for periods 20–50 s, and between 1.2 and 3% (0.6–1.4% standard deviation) for periods 67–125 s (Figure 8a). The values at 100-s period have been omitted because of the large uncertainties associated with the resulting parameters, and because we did not achieve a misfit reduction relative to the isotropic inversion (see Table 1). However, because of the relatively high uncertainties we cannot reject the null hypothesis of isotropy at the 95% confidence level, especially for periods 20–50 s. This result suggests that at shallower depths the magnitude of the regional azimuthal anisotropy is small or variable in direction so that effective anisotropy is low. Significant seismic anisotropy is observed at periods longer than 50 s, indicating that its source is likely located at depths greater than ~100 km (see Figure 3c). For periods greater than 50 s, a degree of anisotropy of about 1–3% agrees with regional estimates of *Nishimura and Forsyth* [1988] that show azimuthal variations of 1–2%.

[29] The direction of fast Rayleigh wave propagation is generally close to east-west (73–101°), comparable with the easterly direction of Nazca plate motion in the hot spot reference frame (90.1° azimuth at 0°N, 91°W, for HS3-NUVEL1A) [*Gripp and Gordon*, 2002]. At 25- and 29-s period the fast direction of propagation changes to almost N-S (14 ± 9° and 9 ± 51°, respectively), close to the direction of Nazca-Cocos spreading (7.15° at 1°N, 91°W, for NUVEL-1A) [*DeMets et al.*, 1994]. However, because only two period bands show this anomalous direction, and because of the high uncertainty of the measured azimuth for the 29-s band and the low degree of anisotropy at lesser periods, we consider that the predominant direction of azimuthal anisotropy in the region is east-west (E-W). We could not resolve lateral variations of anisotropy, and thus our results are average estimates of azimuthal anisotropy for the entire region, which includes the Galápagos platform and its surroundings (Figure 6). However, SKS splitting indicates that anisotropy within the Galápagos platform varies laterally, with isotropy in the center of the archipelago and anisotropy with nearly E-W fast directions along the western edge (81°–109° at seismic stations G05, G06, G07, and G10) [*Fontaine et al.*, 2005]. Regional observations of Rayleigh wave 2θ azimuthal anisotropy across the eastern Pacific also indicate an E-W fast direction of anisotropy [*Nishimura and Forsyth*, 1988; *Montagner and Tanimoto*, 1990]. We suggest that the observed Rayleigh wave azimuthal anisotropy represents an average between an E-W direction of regional mantle flow and isotropy beneath the center of the archipelago.

[30] In a third set of inversions, we obtain lateral variations in phase velocity, but we do not allow for azimuthal anisotropy. We solve for isotropic phase velocity, B_0, at each grid node, while including two-dimensional sensitivity kernels. We use the value of B_0 from the uniform velocity inversions as the initial value in the two-dimensional

Table 1. Comparison of Phase Velocity Inversions

Period (s)	Number of Events	Number of Observations	RMS Phase Misfit (s)		
			Uniform Velocity, No Anisotropy	Uniform Velocity, Uniform Anisotropy	Two-Dimensional Velocity, No Anisotropy
20	94	1330	0.64	0.62	0.51
22	110	1498	0.58	0.53	0.51
25	123	1636	0.71	0.62	0.59
29	119	1584	0.89	0.78	0.69
33	118	1660	0.68	0.63	0.62
40	120	1564	0.79	0.72	0.68
50	120	1540	0.85	0.80	0.77
67	110	1394	0.93	0.87	0.86
80	88	1114	0.83	0.81	0.83
100	76	912	0.82	0.82	0.78
111	69	828	0.92	0.88	0.86
125	63	734	1.01	0.97	0.92

inversions. We also tested the use of a two-dimensional perturbational model resulting from adopting the inversion solution at one period as the initial model for nearby periods (e.g., Weeraratne et al., Rayleigh wave tomography beneath intraplate volcanic ridges in the South Pacific, submitted to Journal of Geophysical Research, 2007), and we confirmed that our results are independent of the starting model. The results of two-dimensional inversions show significant improvement (up to 40% variance reduction) when compared with the uniform isotropic and anisotropic phase velocity inversions, suggesting that lateral variations of phase velocity are required by the data. The resulting phase velocities vary laterally by up to ±1.5% with respect to the uniform phase velocity model (Figure 9). However, phase velocities are consistently lower than values for Pacific lithosphere of comparable ages: 0 to 3% lower than 0–4NF89, and 2 to 9% lower than 4–20NF89. By examining the a posteriori model covariance matrix and the values of uncertainties in model parameters we define an area of best path coverage and resolution, which is used to plot the phase velocity maps in Figure 9.

[31] There are two main regions of anomalously low phase velocity. The first is near the southwestern corner of the archipelago, beneath the volcanoes of Fernandina and southern

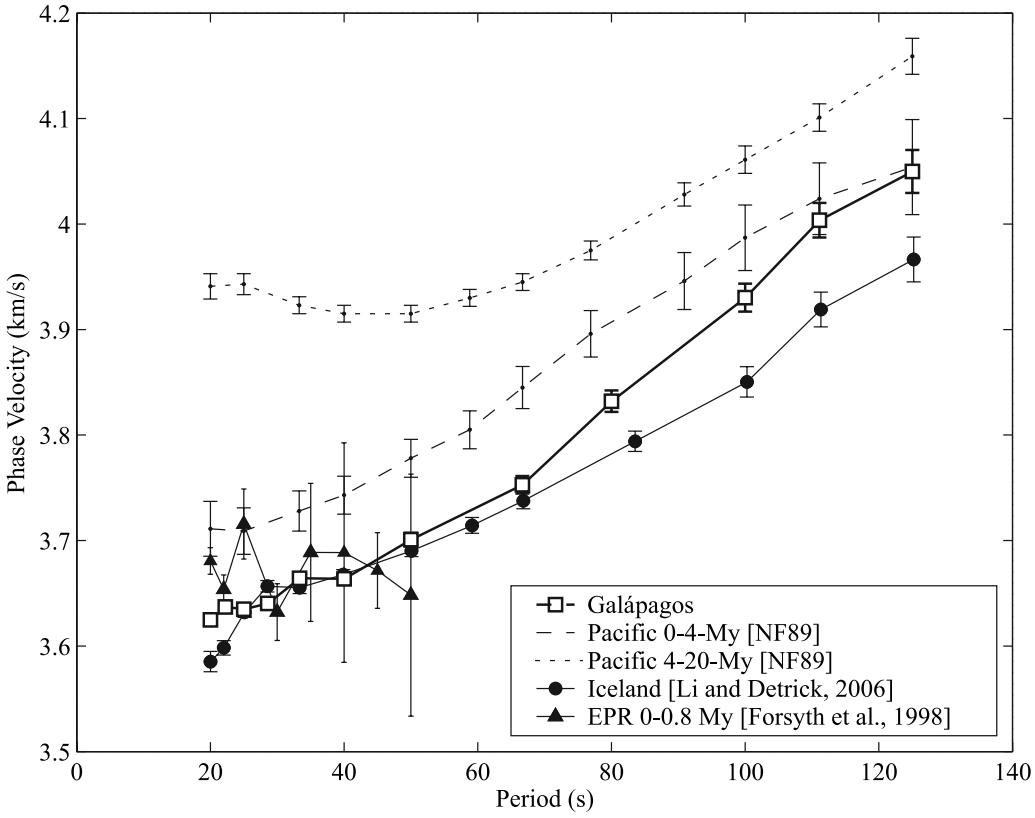

Figure 7. Average phase velocity as a function of period for the Galápagos Archipelago (white squares and bold line). Dashed and dotted lines indicate results from the study of *Nishimura and Forsyth* [1989] for Pacific Ocean lithosphere of age 0–4 My and 4–20 My old, respectively. Circles indicate results from the study of *Li and Detrick* [2006] for Iceland. Triangles indicate results from the study of *Forsyth et al.* [1998] for the East Pacific Rise. All error bars represent one standard deviation.

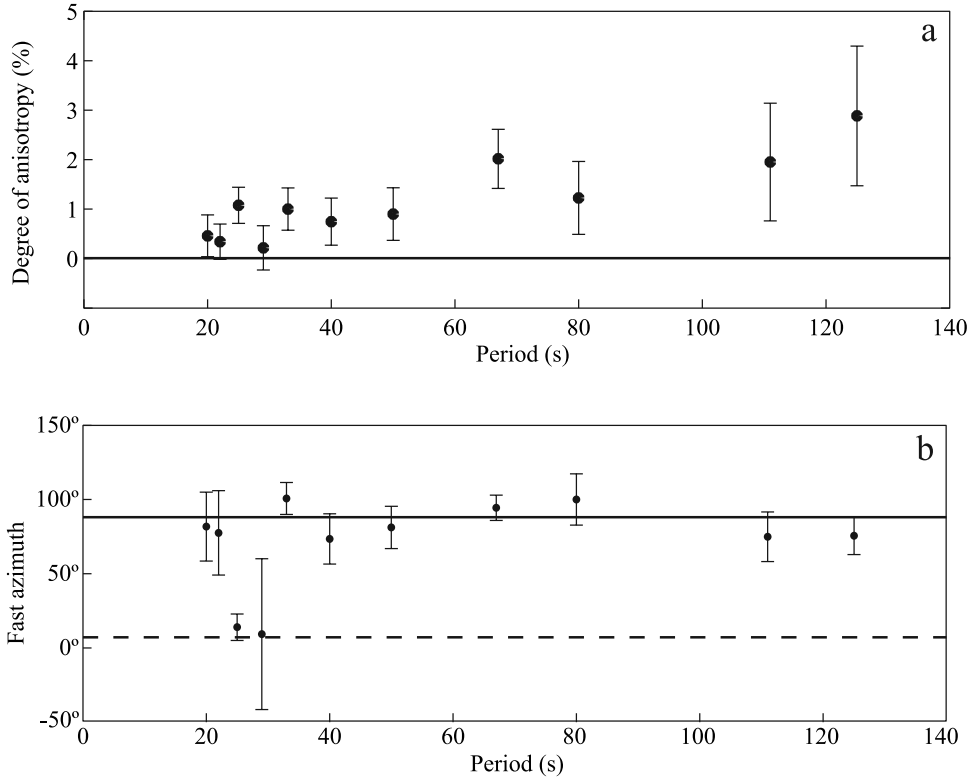

Figure 8. Results from inversions with azimuthal anisotropy. (a) Amplitude of anisotropy as a function of period and 1-σ error bars. (b) Azimuth of fast direction of propagation and 1-σ error bars. The solid horizontal line indicates the direction of plate motion in a hot spot reference frame (89.4° at 0°N, 91°W, for HS3-NUVEL1A) [*Gripp and Gordon*, 2002]. The dashed horizontal line indicates the direction of Nazca-Cocos spreading (7.15° at 1°N, 91°W, for NUVEL-1A) [*DeMets et al.*, 1994].

Isabela. The anomaly is more evident at shorter periods, especially 20–25 s. The second low-velocity region is centered near 0.5°S, 90.5°W, beneath Santiago and Santa Cruz and is evident in the phase velocity maps from 29- to 80-s period. At 100- to 125-s period, the second anomaly decreases in intensity and moves slightly southward.

[32] In a fourth set of inversions, we assume uniform anisotropy but allow for lateral variation in phase velocity. The two-dimensional phase velocities (B_0) vary by less that 0.3% compared with the isotropic case. The amplitude of anisotropy and the direction of fast propagation are also very similar to those obtained in the inversions with uniform phase velocity: the direction of fast propagation varies between 71 and 93°, except at 25-s and 29-s periods, where the direction of anisotropy is 19 ± 7° and 11 ± 74°, respectively, and the peak-to-peak amplitude of anisotropy varies between 0.15 and 2.9%. However, the results of these inversions do not provide significant variance reduction with respect to the isotropic case.

4.3. Shear Wave Velocity Inversion

[33] We use the two-dimensional isotropic phase velocities (third set of inversions) to construct three-dimensional images of shear wave velocity structure. Phase velocity data at each grid node are first inverted for one-dimensional V_S. We then parameterize a one-dimensional model (0- to 410-km depth) in layers of 5-km thickness and use σ_i = 0.1, Δ = 10 km. Last, we merge all the resulting one-dimensional V_S models to obtain the three-dimensional velocity structure following the procedure described in section 3.2. We apply lateral smoothing while allowing for changes of less than 10% of the standard deviation.

[34] The smooth form of the phase velocity kernels (Figure 3c) shows that surface waves cannot resolve sharp vertical velocity changes, including the expected variations at the crust-mantle interface. Crustal velocity structure and thickness estimates are, however, available for the Galápagos platform [*Feighner and Richards*, 1994; *Toomey et al.*, 2001]. We tested the results of the inversion with three different assumptions about the crustal structure. Under the first assumption we use a constant crustal thickness of 15 km and an average crustal velocity profile [*Toomey et al.*, 2001] as our initial model. Changes with respect to these initial crustal velocities are penalized more than changes of mantle velocities in the inversion (σ_i = 0.01 versus σ_i = 0.1, respectively). Because we expect bathymetric depth to be negatively correlated with crustal thickness, under the second assumption we assign different crustal thicknesses to different grid nodes as a function of bathymetry: crustal thickness is taken to be 5 km if bathymetric depth is greater than 2000 m, 10 km if bathymetric depth is between 2000 and 1000 m, and 15 km otherwise. Again, changes with respect to the initial crustal velocities are penalized more than changes of mantle velocities in the inversion (σ_i = 0.01 versus σ_i = 0.1, respectively). The third assumption is that crustal thickness and velocities are nowhere constrained (σ_i = 0.1 everywhere). We find that changing the assumption about crustal structure has no significant

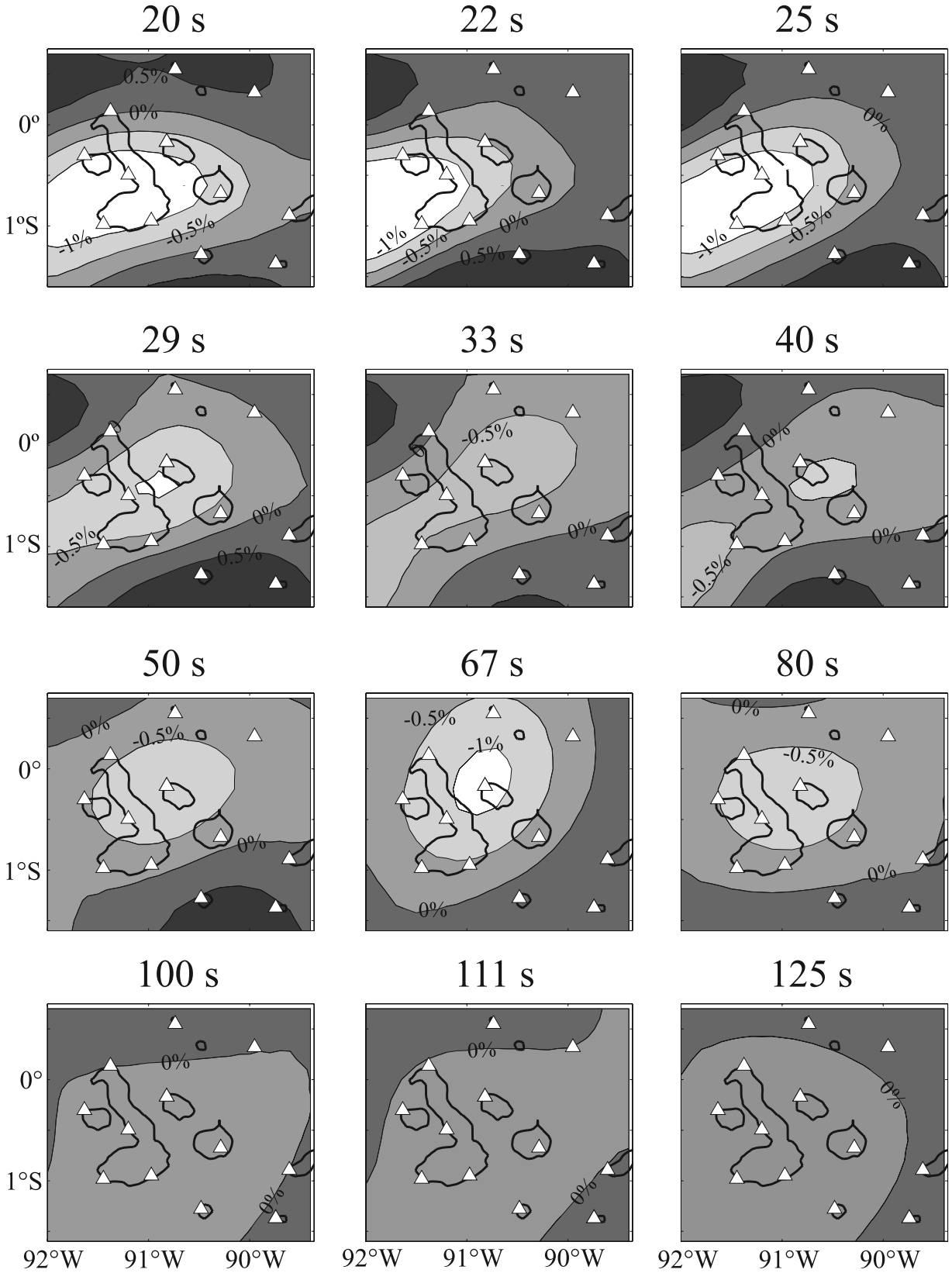

Figure 9. Results of inversion for two-dimensional isotropic phase velocity for all period bands. Units are percent variation with respect to the frequency-dependent value of the isotropic uniform phase velocity (from Figure 7). Contours shown are −1, −0.5, 0, and 0.5%. Thick lines outline the Galapagos Islands (0-m isobath), and white triangles indicate the locations of seismic stations.

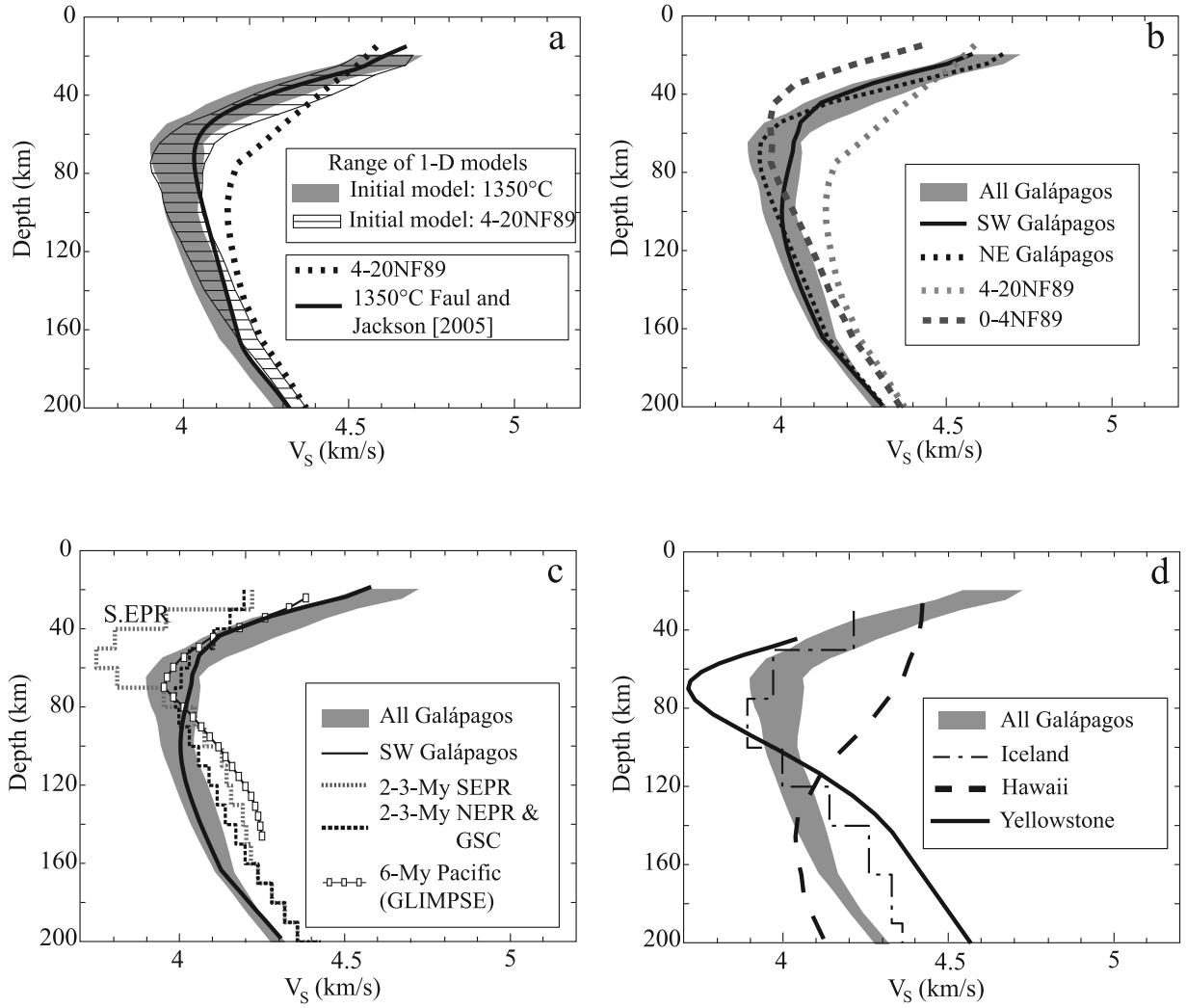

Figure 10. Results of inversions for shear wave velocity. (a) Range of one-dimensional V_S models as a function of depth for two inversions using different initial models. Gray area indicates one-dimensional V_S range for an initial model derived from a 1350°C adiabat [*Faul and Jackson*, 2005] (solid line). Hatched area represents one-dimensional V_S range with 4–20NF90 (dotted line) as the initial model. (b) Comparison of Galápagos one-dimensional V_S models (gray area from Figure 10a) and average velocities for the southwestern (black solid line) and northeastern (black dotted line) parts of the archipelago with 0–4NF89 (dashed gray line) and 4–20NF89 (dotted gray line). (c) Comparison of Galápagos one-dimensional V_S models (gray area from a) with Pacific V_S models. Solid lines indicate 2- to 3-My-old EPR and GSC from *Gu et al.* [2005]. White squares show a model for the mantle beneath intraplate volcanic ridges on 6-My-old south Pacific seafloor [Weeraratne et al., 2007]. (c) Comparison of Galápagos one-dimensional V_S models (gray area from a) with V_S models for other hot spot regions. Dash-dot line indicates the ICAV model for Iceland [*Allen et al.*, 2002], dashed line shows a V_S model for Hawaii [*Priestley and Tilmann*, 1999; *Tilmann*, 1999], and solid line indicates a model for Yellowstone (D. Schutt and K. Dueker, Excess temperature of the Yellowstone plume, manuscript in preparation).

an effect on velocities deeper than ~40 km; at shallower depths the magnitudes of the velocity anomalies change but their locations remain stable.

[35] We also tested the dependence of the inversion on the mantle starting model by performing inversions using several different initial mantle velocity profiles: the isotropic part of V_S from 4–20NF89 and models constructed from different mantle adiabats and lithospheric ages using the methodology of *Faul and Jackson* [2005]. As an example, Figure 10a shows the range of resulting one-dimensional V_S models we obtain using two different initial models (gray and hatched areas). In general, we find little dependence of the results on the initial velocity model, especially for the depth range from 60 to 150 km. In what follows we discuss only those aspects of structure that are insensitive to the initial crustal and mantle velocity models.

[36] The results of the one-dimensional V_S inversions with bathymetry-dependent crustal thickness are shown in Figure 10. The hatched area in Figure 10a corresponds to the range of models obtained using the isotropic part of V_S from 4–20NF89 as an initial model. The gray area in Figures 10a–10d corresponds to the range of models

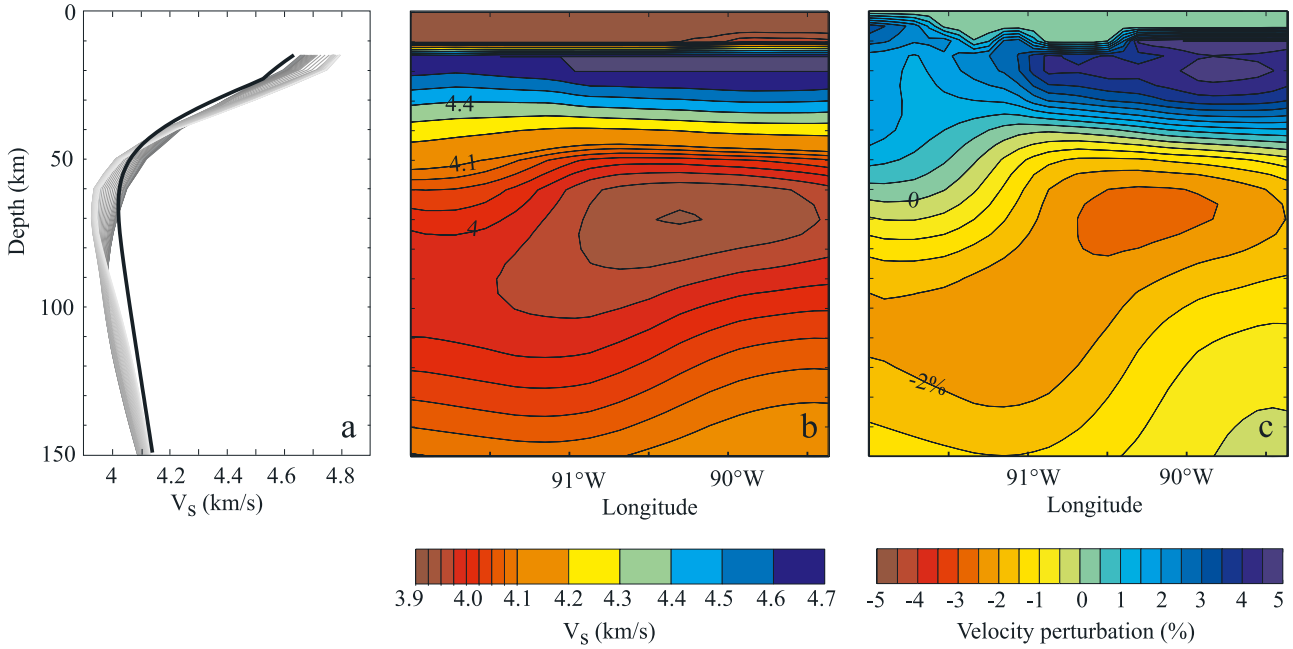

Figure 11. One-dimensional V_S models and E-W cross sections of the three-dimensional V_S model at latitude 0.2°S. (a) Gray lines indicate the range of one-dimensional V_S models, and the black line shows the reference model (1350°C adiabat, 10-My-old lithosphere, and 2-mm grain size). Gray lines go from darker to lighter from west to east. (b) Absolute V_S in kilometer per second. (c) Velocity perturbation in percent relative to the reference model.

obtained using an initial model resulting from a 1350°C mantle adiabat, 10-My-old lithosphere, and 2-mm grain size [*Faul and Jackson*, 2005]. For this range of one-dimensional models, the lowest V_S is 3.9 km/s at 65-km depth. This value is lower than those estimated beneath most young regions in the Pacific: 0–4NF89, 4–20NF89 (Figure 10b), and 2- to 3-My-old lithosphere near the northern East Pacific Rise (EPR) or GSC [*Gu et al.*, 2005] (Figure 10c). However, it is ~4% higher that V_S at 50- to 60-km depth beneath 2- to 3-My-old lithosphere near the southern EPR [*Gu et al.*, 2005] (Figure 10c). Nonetheless, the estimates of *Gu et al.* [2005] for the southern EPR were made in a direction parallel to the ridge, in the slow direction of wave propagation [*Wolfe and Solomon*, 1998]. Thus it is possible that some of the anomalously low velocities imaged at 50- to 60-km depth near the southern EPR represent the effects of seismic anisotropy, and that the mean V_S is higher.

[37] Between 50- and 110-km depth, the average velocities in the southwestern part of the archipelago are up to 2.5% higher than those in the northeast (Figure 10b). The average velocities in the southwestern Galápagos are also higher than those of 0–4NF89 and other young regions in the Pacific at depths shallower than ~80 km (Figures 10b and 10c). Deeper than 100 km, both the mean and minimum V_S values beneath the entire Galápagos region are consistently lower than those beneath young Pacific seafloor elsewhere (Figures 10b and 10c).

[38] When compared with other oceanic hot spots (Figure 10d) velocities beneath the Galápagos are comparable to mantle velocities beneath Iceland [*Allen et al.*, 2002] between 40- and 120-km depth, but lower than for Icelandic mantle deeper than 120 km. Velocities are higher (by up to 0.2 km/s) than for sublithospheric mantle beneath Hawaii [*Priestley and Tilmann*, 1999; *Tilmann*, 1999] at depths between ~120 and 200 km. When compared with shallow mantle beneath Yellowstone (D. Schutt and K. Dueker, Excess temperature of the Yellowstone plume, manuscript in preparation, 2007), the Galápagos is seismically faster at depths shallower than ~100 km, but significantly slower at greater depths (Figure 10d).

[39] In Figures 11, 12, and 13 we show the three-dimensional shear wave velocity anomalies constructed from the one-dimensional V_S models. Velocity anomalies are relative to the initial model corresponding to a 1350°C adiabat, which we term the reference model (black line in Figure 11a). Figure 11 shows a comparison of results as absolute shear velocity (Figure 11b) and velocity perturbations (Figure 11c) along an E-W cross section at 0.2°S. In what follows we present the three-dimensional V_S model as velocity perturbations; choosing a different reference model or showing the values of absolute velocity instead do not change the results discussed below. In map view (Figure 12), we distinguish a continuous region of anomalously low velocity between 50- and 150-km depth (Figures 12b–12f).

[40] Deeper than 100 km the lowest velocities (1–2% lower than the reference model) are localized north of 0.5°S and west of 90.5°W, beneath Fernandina and northern Isabela (Figures 12e–12f). Low velocities at these depths also extend to the north and northwest, toward the edge of the region of best path coverage. Spatially, this anomaly correlates well with the volcanoes of Fernandina and Isabela that are among the youngest and largest edifices in the archipelago, and where basalts show higher amounts of enrichment of incompatible elements [e.g., *White et al.*, 1993; *Harpp and White*, 2001] and $^3He/^4He$ [*Kurz and Geist*, 1999]. In addition, the lowest velocities at these

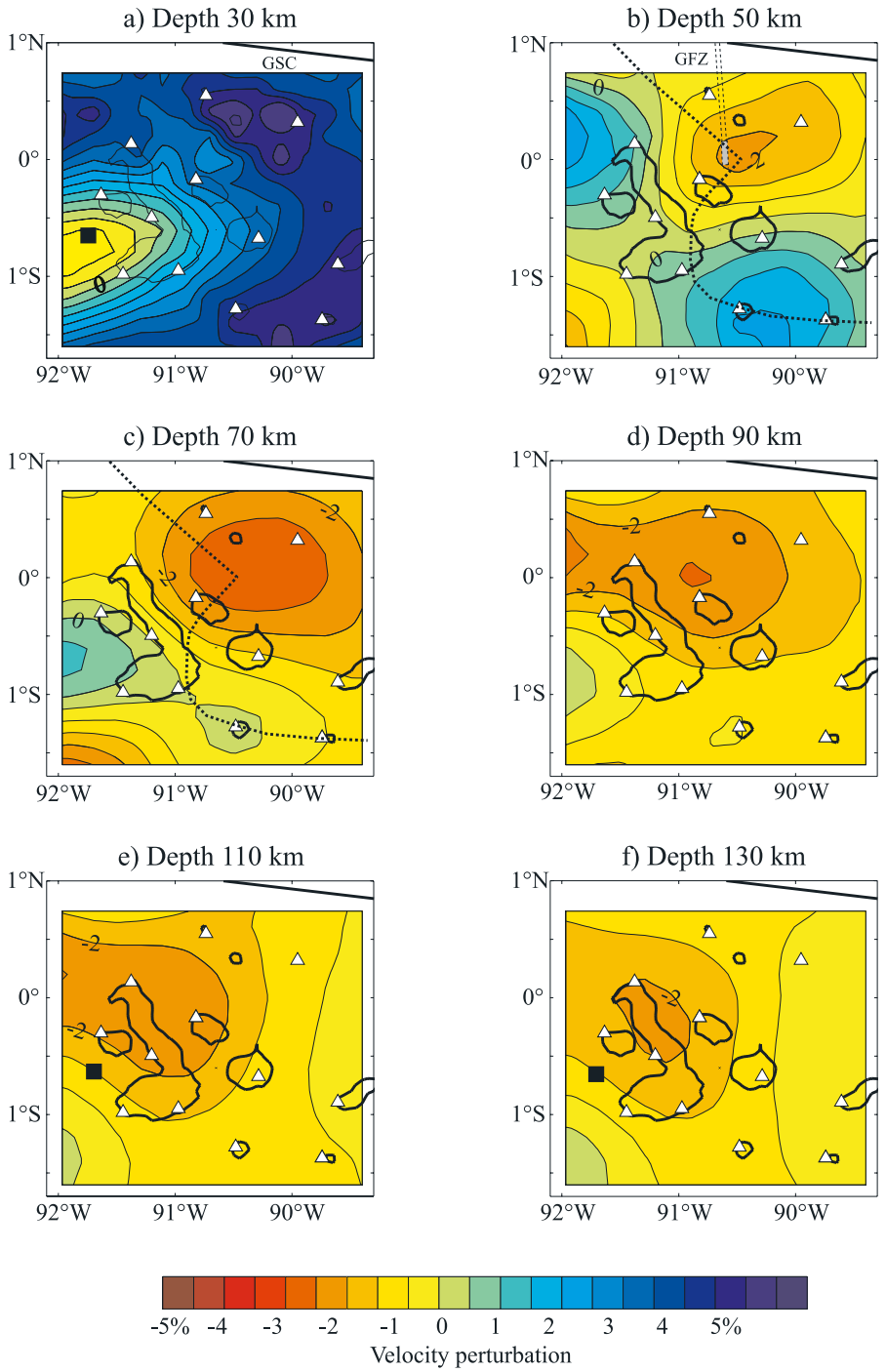

Figure 12. Shear wave velocity perturbation at depths of 30, 50, 70, 90, 110, and 130 km. Units are percent variation with respect to the reference model. Contours are at 0.5% increments (0 and −2%% contours are labeled). Thick lines delineate the Galapagos Islands (0-m isobath), and white triangles indicate the locations of seismic stations. Bold straight line to the north indicates the position of the Galápagos Spreading Center (GSC). Dashed double line in Figure 12b shows the Galápagos Fracture Zone (GFZ). Gray area in Figure 12b shows the southern extent of the GFZ assuming a maximum age of 3.6 My [*Wilson and Hey*, 1995] and a half-spreading rate of 25−30 km/My. The heavy dotted line in Figures 12b and 12c indicates the fault-like discontinuity that *Feighner and Richards* [1994] suggest separates weaker lithosphere to the east from stronger lithosphere to the west and south. The black square in Figures 12a, 12e, and 12f represents the center of a downward deflection of the 410-km discontinuity [*Hooft et al.*, 2003].

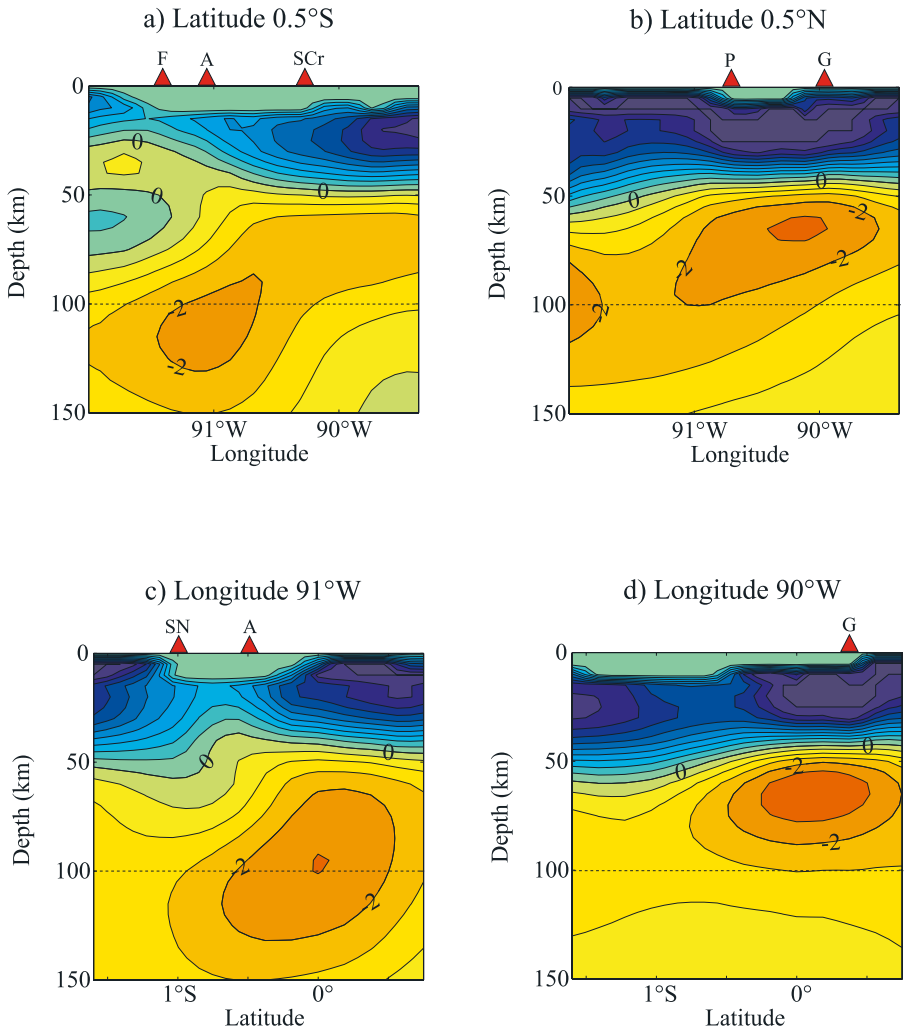

Figure 13. E-W cross sections though three-dimensional V_S model at latitudes (a) 0.5°S and (b) 0.5°N, and N-S cross sections at longitudes (c) 91°W and (d) 90°W. Color scale and contours as in Figure 10. Red triangles indicate approximate locations of volcanoes: SN, Sierra Negra; F, Fernandina; A, Alcedo; P, Pinta; G, Genovesa; and SCr, Santa Cruz.

depths within this anomalous region lie north-northeast of the center of a downward deflection of the 410-km discontinuity [*Hooft et al.*, 2003] (black square in Figure 12f) and above a low-velocity anomaly detected by body wave imaging at depths of 100–200 km [*Toomey et al.*, 2002a].

[41] Between 100- and 80-km depth, the low-velocity volume broadens in the E-W direction and intensifies toward the north, east, and west (Figure 12d); this intensification may in part result from enhanced resolution at shallower depths, as discussed below. Between 80- and 50-km depth, the lowest velocities (1.5–2.5% lower than reference model) are centered at 0°N, 90.5°W, beneath the islands of Genovesa, Pinta, Marchena, and Santiago (Figures 12b and 12c). At these depths, the anomaly intensifies east of the 91°W Fracture Zone (Figure 12b). This low-velocity anomaly also underlies a region that erupts depleted basalts with decreased contributions of hot spot-related incompatible elements [*Harpp and White*, 2001). Recent volcanic activity in this part of the archipelago is also less intense than in the western part, with less frequent eruptions and smaller volcanic edifices. *Feighner and Richards* [1994] suggest that the lithosphere is weaker and possibly thinner in this region on the basis of gravity and bathymetry data (Figures 12b and 12c).

[42] A second low-velocity region (0–1.2% lower than reference model) is seen at shallow depths (between 20 and 40 km) in the southwestern corner of the archipelago (Figure 12a). This anomaly, which lies near Fernandina and southwestern Isabela and toward the edge of the area of good path coverage, lies above the center of the deflection of the 410-km discontinuity [*Hooft et al.*, 2003] (black square in Figure 12a) and a low-velocity anomaly imaged using *S* wave delays [*Toomey et al.*, 2002a].

[43] Figure 13 displays vertical cross sections though our three-dimensional V_S model. East-west cross sections (Figures 13a and 13b) show a continuous low-velocity anomaly that extends from the bottom of our model to ~40–70 km depth. Deeper than 100 km the lowest velocities are located near 91°W and are approximately confined to the west of 90.5°W (Figure 13a). At 0.5°N the anomaly broadens to the west at ~100-km depth and to the east between 100- and 50-km depth (Figure 13d).

[44] North-south cross-sections (Figures 13c and 13d) show that near 91°W the lowest velocities deeper than 100 km are located north of 1°S. At that longitude the lowest velocities are inclined from south to north as they shoal: 150-km depth at 0.5°S to 100-km depth at 0° latitude (Figure 13c). At 90°W the anomalously low velocities are confined above 100-km depth (Figures 13b and 13d).

[45] The top of the low-velocity anomaly appears as a sharp velocity change. This boundary is present everywhere beneath the archipelago at depths from 40 to 70 km (for example, ~4.0 km/s or 0% contours in Figures 11b and 11c, respectively). The boundary is deepest beneath the southwestern part of the archipelago and shoals and sharpens toward the east and north, with a more or less abrupt transition near 91.2°W in the E-W direction (Figure 13a) and 0.5°S in the N-S direction (Figure 13c).

4.4. Model Resolution

[46] Fundamental Rayleigh waves are sensitive to structure as deep as one wavelength; thus the range of frequencies used in this study could potentially provide information about structure in the entire upper mantle, to a depth of 410 km. However, resolution decreases greatly with depth, and therefore we expect that only shallow features in the upper mantle are well resolved. To test this presumption, and to test how well the depth of a sharp velocity contrast is resolved, we ran a series of inversions using synthetic three-dimensional V_S models (see Appendix A).

[47] In general, shear wave velocity anomalies were well recovered between 30- and 80-km depth. Between 80- and 150-km depth the resolving power decreases considerably, and toward the bottom of the model (deeper than ~110 km) velocity anomalies are smeared laterally and the amplitudes can be underestimated by up to a factor of 4 for anomalies with lateral extents of less than 200 km. We assign 150 km as a maximum depth of acceptable resolution. We conclude that while the precise shapes and amplitudes of anomalies are difficult to resolve, their sign and general location are well resolved between 30- and 150-km depth.

5. Properties of the Upper Mantle

[48] Our model of shear wave velocity constrains the physical and chemical properties of the mantle beneath the Galápagos region. We first address excess temperature and melt fraction at depths of 75 to 150 km. We then examine the origin of the high-velocity lid to assess whether it is related to the formation of thermal lithosphere or to compositional variations associated with melt extraction.

5.1. Properties at 75- to 150-km Depth

[49] Shear wave velocities beneath the Galápagos at depths between 75 and 150 km are lower than those beneath other region of comparable age in the Pacific (Figures 10b and 10c), suggesting that a hotter-than-normal asthenosphere underlies the Galápagos. To estimate excess mantle temperature we follow the approach of Schutt and Dueker (Excess temperature of the Yellowstone plume, manuscript in preparation, 2007). We use the model of *Faul and Jackson* [2005], which incorporates laboratory measurements of shear modulus and attenuation made on melt-free polycrystalline olivine. Predictions of this model are dependent on grain size, temperature, activation volume (V^*), and activation energy (E^*).

[50] We chose the depth range 75 to 150 km because it is everywhere below the high-velocity lid imaged in the inversions and lies mostly within the damp melting region where melt fraction is likely small. Resolution tests show that we recover only 25–50% of the velocity anomalies in this depth range, so the results are minimum estimates of excess mantle temperature.

[51] We first calculate one-dimensional V_S models as functions of mantle potential temperature and grain size for given values of activation energy and activation volume. We assume an adiabatic temperature profile in the asthenosphere and a half-space cooling model for the lithosphere. We search for the models that best fit the results of our inversions, which permits us to bracket probable ranges in mantle temperature. Using estimates of normal mantle potential temperature, we then convert the temperature ranges to excess mantle temperature. Estimated values of potential temperature of normal mantle are 1280°C [*McKenzie and Bickle*, 1988], 1330°C [*White et al.*, 1992], and 1350°C [*White and McKenzie*, 1995]. Hereafter we choose the highest estimate of 1350°C as the nominal mantle potential temperature.

5.1.1. Effect of Temperature

[52] We first constrain likely ranges of mantle potential temperature beneath the Galápagos region by assuming that the velocity variations are caused by temperature differences alone. Since there is a trade off between upper mantle temperature and grain size on shear velocity these two parameters cannot be independently constrained from a given V_S. For example, a higher potential temperature can be compensated by a correspondingly larger grain size. Grain size in the upper mantle is on the order of 1–10 mm [*Hirth and Kohlstedt*, 2003; *Faul and Jackson*, 2005]. *Faul and Jackson* [2005] found that models for oceanic upper mantle with a 1300°C potential temperature and a constant grain size of 1 mm provide a good fit to the results of *Nishimura and Forsyth* [1989] for the upper 165 km in the Pacific.

[53] We constructed one-dimensional V_S models for mantle potential temperatures between 1200 and 1600°C, average grain size between 1 and 10 mm, and $V^* = 12$ cm^2/mol. A comparison of our inversion results with theoretical models derived for 1350 and 1450°C potential temperatures and 2 and 10 mm grain sizes is shown in Figures 14a and 14c. Model predictions of attenuation are shown in Figures 14b and 14d.

[54] We first used a value of $E^* = 450$ kJ/mol derived from laboratory experiments [*Karato*, 1993]. For an average grain size of 2 mm, estimates of temperature beneath the Galápagos region at depths between 75- and 150-km range from 1350 to 1450°C (bold and thin solid lines in Figure 14a, respectively). Estimates of mantle potential temperature are greater for a grain size of 10 mm (dashed lines in Figure 14a). However, model predictions using $E^* = 450$ kJ/mol do not match attenuation as given by the PREM model [*Dziewonski and Anderson*, 1981] or as observed in other regions of young Pacific seafloor [*Ding and Grand*, 1993; Yang et al., Seismic attenuation near the East Pacific Rise and the origin of the low-velocity zone, submitted to Earth and Planetary Science Letters, 2007, hereinafter referred to as Yang et al.,

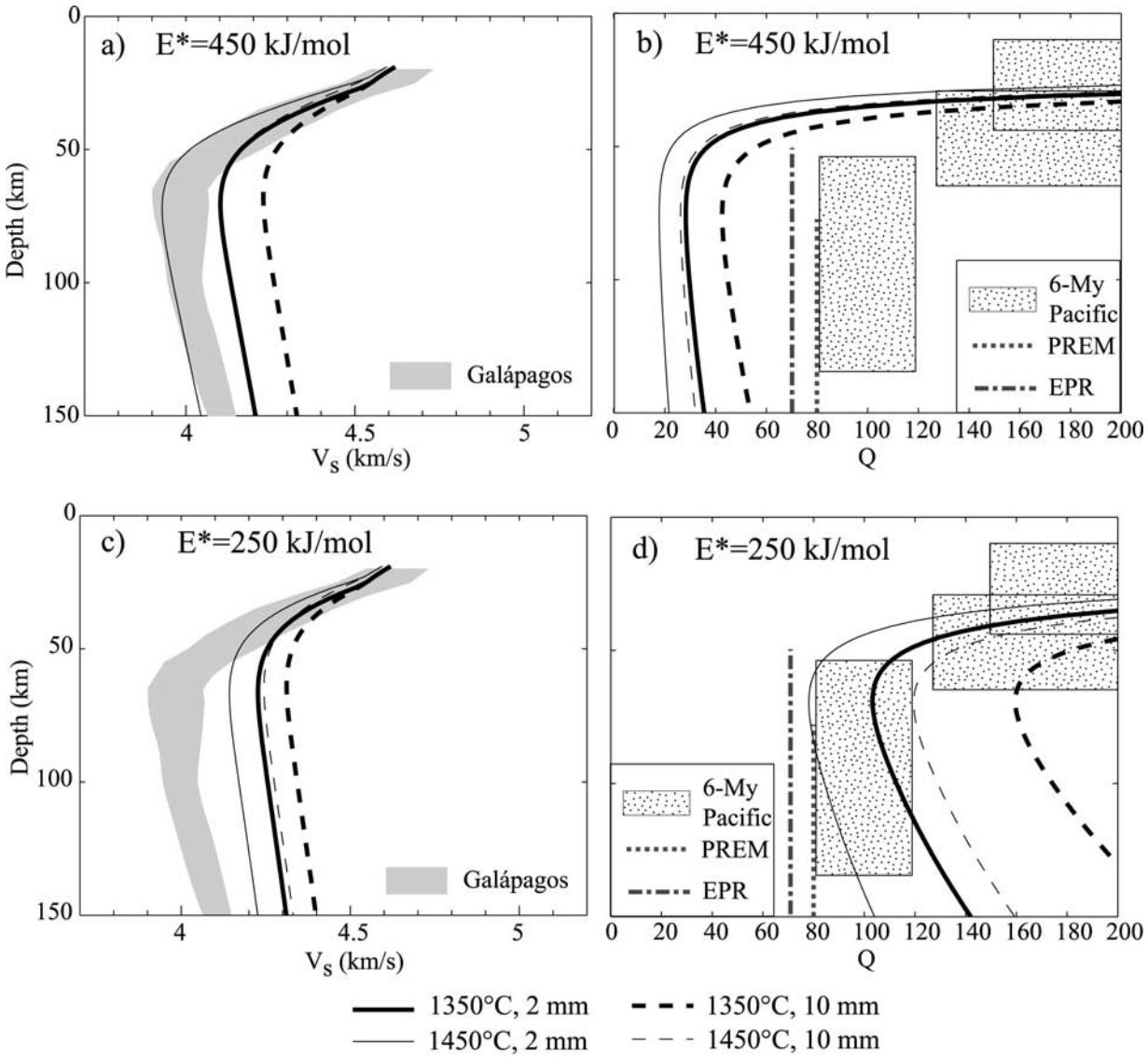

Figure 14. Comparison of one-dimensional V_S models with models calculated using the methodology of *Faul and Jackson* [2005] for potential temperatures of 1350°C (bold lines) and 1450°C (thin lines) and grain size of 2 mm (solid line) and 10 mm (dashed line). (a and c) Comparison of Galápagos V_S model (gray area) with model predictions using (a) E^* = 450 kJ/mol and (c) E^* = 250 kJ/mol. (b and d) Comparison of model prediction of attenuation and seismic observations from PREM [*Dziewonski and Anderson*, 1981] (dotted line), EPR [*Ding and Grand*, 1993] (dash-dotted line), and 6-My-old Pacific from the GLIMPSE experiment [Yang et al., 2007] (dot-patterned areas) with (b) E^* = 450 kJ/mol and (d) E^* = 250 kJ/mol.

submitted manuscript, 2007] (Figure 14b). An alternative is to use a lower value of E^* = 250 kJ/mol that matches seismic observations of Q (Figure 14d), as suggested by Yang et al. (submitted manuscript, 2007), but which gives estimates of excess mantle temperature that are 200 to 300°C higher (Figure 14c). For the following analysis we chose the laboratory estimate of E^* = 450 kJ/mol because it predicts conservative values of potential temperature. We note that our estimates of excess mantle temperature are thus minimum estimates.

[55] A comparison of observed V_S beneath the Galápagos region between 75 and 150 km depth and model predictions using the nominal potential temperature of 1350°C confirms that the asthenosphere shows anomalously low velocities (Figure 14a). Velocity reduction varies from 0.5 to 2.5% (5 to 7%) for a grain size of 2 mm (10 mm). Figure 15a shows the results of comparing the observed V_S beneath northern Isabela (where the lowest velocities are found at depths greater than 75 km) and all the calculated V_S models for grain sizes from 1 to 10 mm. The estimated potential temperature beneath northern Isabela is 1400°C (1550°C) for 1-mm (10-mm) grain size (stars in Figure 15a). The uncertainties in these values are approximately ± 20°C (30°C) for 1-mm (10-mm) grain size from the 95% χ^2 estimates (black contour in Figure 15a).

[56] We repeat this process for each one-dimensional V_S model. The results are summarized in Figure 15b. Assuming no melt effects, the best estimates of potential temperature

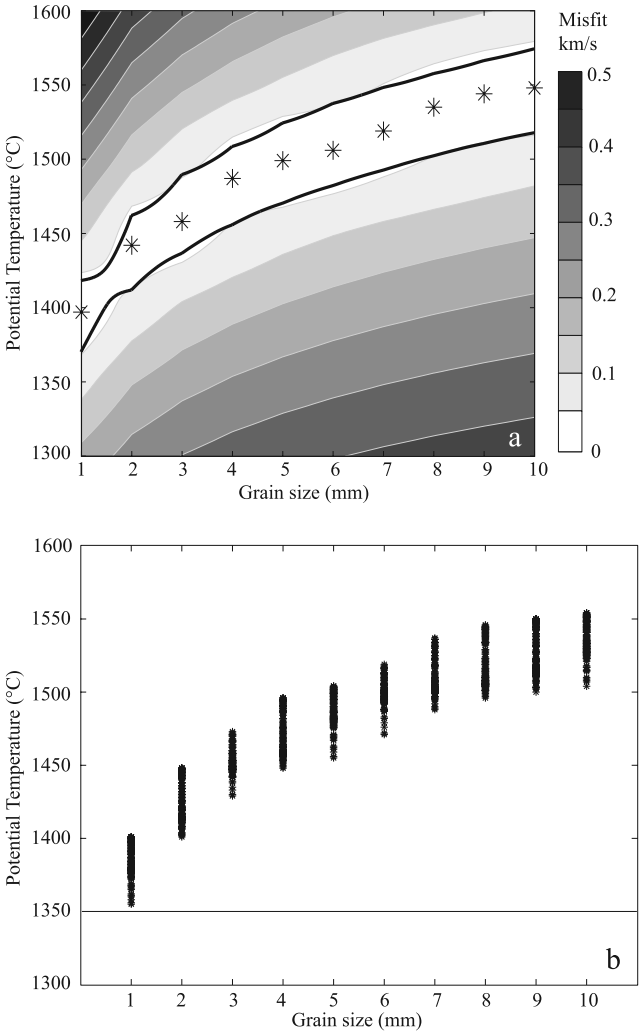

Figure 15. Best fitting potential temperatures as a function of grain size assuming no melt effects on V_S. (a) Misfit between one-dimensional V_S model beneath northern Isabela from 75- to 150-km depth and calculated models as a function of potential temperature and grain size. The RMS misfit, which characterizes the goodness of fit between the observed V_S and the calculated model, is contoured as a function of potential temperature and grain size. Stars represent best fitting potential temperature for each grain size. Thick solid line indicates 95% χ^2 contour. (b) Best fitting potential temperature as function of grain size for each one-dimensional V_S model beneath the entire region. Horizontal line indicates the 1350°C potential temperature of normal mantle [*White and McKenzie*, 1995].

beneath the Galápagos region range between 1350° and 1400°C (1500° and 1550°C) for a grain size of 1 mm (10 mm), which correspond to a maximum excess mantle temperature of 50°C (200°C). The results also suggest that the range of V_S observed beneath the hot spot could be explained by lateral variations of ~50°C. This analysis takes the tomographic results at face value. However, our analysis of resolution shows that V_S anomalies are underestimated at depths between 75 and 150 km, and thus the results are minimum estimates of variations in potential temperature.

5.1.2. Effect of Melt Fraction

[57] The velocity reduction observed beneath the Galápagos region is likely caused by a combination of melt and excess temperature. Here we consider the effect of partial melt on shear velocity in order to test further our estimates of excess mantle temperature. We assume that the mantle beneath the Galápagos region is buoyant and upwells, leading to decompression melting and that the presence of volatiles initiates melting at temperatures below the dry solidus. Our goal is not to constrain absolute melt fraction, as this is not possible from V_S information alone. Instead, our main interest is to learn if, after effects of melt content are included, the low shear wave velocities still require an elevated mantle potential temperature.

[58] We expect melt content at depths greater than 75 km to be small. Melt productivity in this region of wet melting is low, up to 25–30 times less than in the dry melting region [e.g., *Asimow et al.*, 2004]. Volatile-rich melts could be mobile at these depths even though porosity is very small [*Faul*, 2001]. From a model of one-dimensional porous flow in a network of tubules [*Turcotte and Schubert*, 2002, pp. 402–405] we estimate that the melt fraction could be in the range ~0.05–0.5% at 75-km depth [Appendix B]. Melt content values on the order of 0.1% are also consistent with predictions from trace element and uranium-series disequilibria models of melting at mid-ocean ridges [e.g., *Lundstrom et al.*, 1995]. We consider that for depths greater than 75 km the melt fraction is likely in the range 0.1 to 0.5%.

[59] It is unlikely that the effect of 0.1–0.5% melt on V_S can account for the 2.5% (7%) velocity reduction observed for a grain size of 1 mm (10 mm) (Figure 14a). At low melt fractions (generally less than 0.75–1%) melt is probably contained predominantly in tubules [e.g., *Hammond and Humphreys*, 2000]. With the melt-velocity relations of *Hammond and Humphreys* [2000], $\partial \ln V_S / \partial \phi = -2.7$ for melt that is contained in tubules, so 0.1 to 0.5% melt could produce 0.27 to 1.35% velocity reduction. Even if we assume a melt fraction of 1%, the velocity reduction is only 2.7%. Thus a thermal anomaly is likely at depths greater than 75 km. With a melt fraction of 0.5% between 75- and 150-km depth, our observations require a mantle excess temperature of ~30°C (~150°C) for a grain size of 1 mm (10 mm). We limit this analysis to the lower part of the model because we expect melt fraction to be higher in the dry melting region and the effect of melt on velocity to be more significant. We remark that this analysis was performed using E^* = 450 kJ/mol. A lower value of E^*, as seems to be required by seismic observations of attenuation (Yang et al., submitted manuscript, 2007), would imply a larger temperature anomaly or a larger melt fraction.

[60] We conclude that the anomalously low shear wave velocities detected at depths greater than 75 km are consistent with melt fractions of ~0.5% and elevated temperatures beneath the Galápagos hot spot of 30° to 150°C, depending on average grain size. Our estimate of excess mantle temperature is comparable to values suggested by other studies. The amount of thinning of the transition zone beneath the Galápagos indicates an excess temperature of 130 ± 60 K at 410-km depth [*Hooft et al.*, 2003]; modeling of hot spot-ridge interaction for the GSC suggests 50–100 K excess temperature [*Ito et al.*, 1997]; and modeling of the source of GSC basalts affected by the hot spot indicates

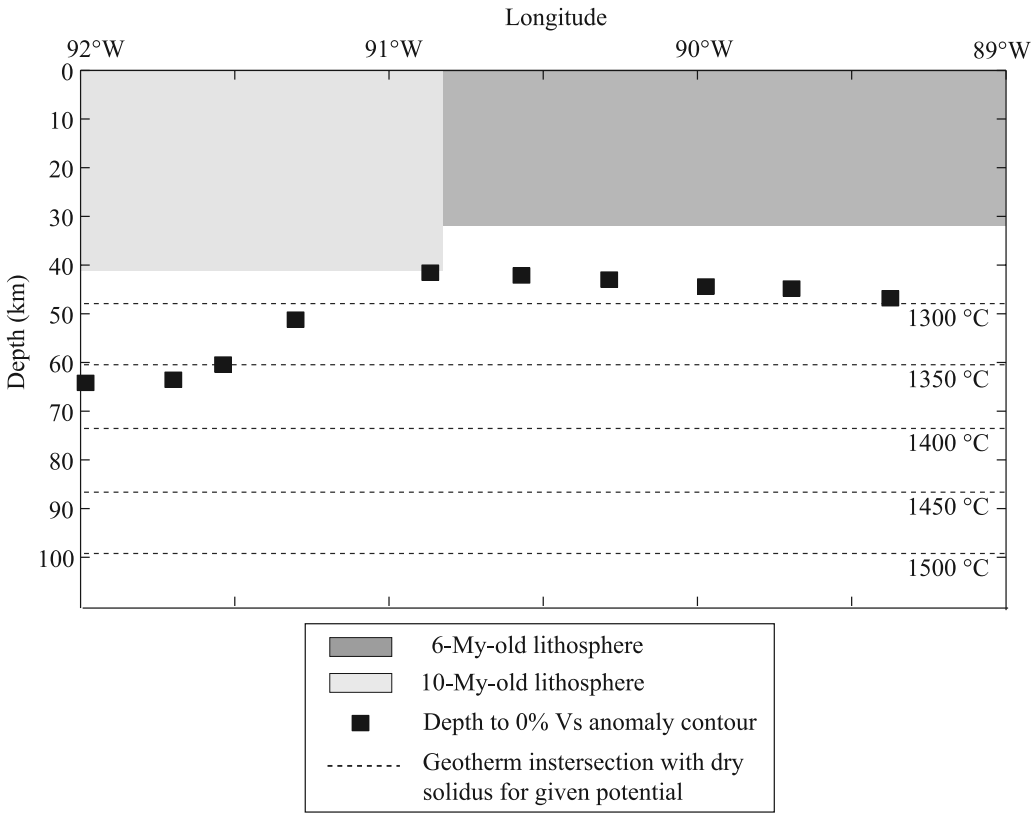

Figure 16. Depth to 0% V_S change contour (squares) along an E-W profile at 0.2°S compared with the likely range in lithospheric thickness derived from a half-space cooling model [*Turcotte and Schubert*, 2002] and the depth to the dry solidus. Lithospheric age across this profile changes from 6 My (dark gray) toward the east to 10 My (light gray) toward the west near 90.5–91°W (southern projection of the GFZ). Dashed lines indicate depth to dry solidus as given by intersection of the analytical solidus of dry peridotite [*McKenzie and Bickle*, 1988] and the mantle geotherm as a function of potential temperature [*Turcotte and Schubert*, 2002].

a mantle potential temperature of 1395°–1420°C or 45–70 K excess temperature [*Asimow and Langmuir*, 2003].

5.2. Properties at Less Than 75 km Depth

[61] In the Galápagos region, the top of the anomalously low velocity volume is defined by a relatively sharp velocity contrast located between 40- and 70-km depth everywhere beneath the archipelago (Figures 11 and 13). Resolution tests indicate that the depth of this boundary is known to within 5 to 10 km (see Appendix A). The base of this high-velocity lid is deepest beneath the southwestern part of the archipelago and shoals toward the north and east.

[62] Two possible boundaries that could be located at these depths are the bottom of the thermal lithosphere and a compositional boundary related to either depletion or dehydration resulting from melt extraction. The high-velocity lid is thicker to the west of 91.2°W and thins to the north, as expected for thermal lithospheric thickness in the region. In addition, the high-velocity lid is thinner in the northeastern part of the archipelago, roughly matching the region of weaker and thinner lithosphere of *Feighner and Richards* [1994]. However, estimates of thermal lithospheric thickness beneath the Galápagos region are between 30 and 45 km (calculated for a half-space cooling model and seafloor age between 5 and 15 Ma), significantly less than the 70-km depth of the boundary in the southwestern corner of the archipelago (Figure 16). Thus although we cannot rule out that the boundary corresponds to the bottom of the thermal lithosphere in the eastern archipelago, the boundary appears to be ~30 km too deep in the southwest. Anomalously, high velocities beneath the southwestern archipelago at depths from 50 to 70 km are also indicated by comparisons of one-dimensional velocity profiles. Between 50 and 110 km depth, the average velocities in the southwestern part of the archipelago are up to 2.5% higher than those in the northeast (Figure 10b), and higher than those of 0–4NF89 and other young regions in the Pacific at depths shallower than ~80 km (Figures 10b and 10c).

[63] Our preferred explanation is that the anomalously high velocities imaged beneath the southwestern archipelago between 50- and 70-km depth correspond to a compositional change produced during melt extraction beneath the hot spot. The amplitude of the southwestern velocity anomaly is about +3%, following *Faul and Jackson* [2005] and for a potential temperature of 1400°C (50°C excess mantle temperature). One effect of melt depletion of peridotite is a change in modal mineralogy and major element chemistry, which can increase V_S up to 2.6% in the spinel stability field [*Matsukage et al.*, 2005]. A complementary effect is the removal of water [*Karato*, 1986; *Hirth and Kohlstedt*, 1996;

Karato and Jung, 1998], which decreases anelasticity, leading to lower attenuation of seismic waves and higher seismic wave velocities. We estimate the effect of dehydration using [*Karato*, 1993]

$$V(\omega, T, P, C_{\mathrm{OH}}) = V_0(T, P) \cdot \left[1 - 1/2 \cot(\pi\alpha/2)\, Q^{-1}(\omega, T, P, C_{\mathrm{OH}})\right], \quad (4)$$

where $V_0(T,P)$ is the seismic wave velocity as a function of temperature (T) and pressure (P) when only elastic effects are considered; $Q^{-1}(\omega, T, P, C_{\mathrm{OH}})$ is seismic wave attenuation and is a function of frequency (ω), T, P, and water content (C_{OH}); and the parameter α characterizes the frequency dependence of Q ($Q^{-1} \sim \omega^{\alpha}$). We assume that dehydration increases Q from 80 to ~150 [*Karato*, 2003], an estimate consistent with the observed increase in Q by ~2 when dunite samples are dried prior to measurements [*Jackson et al.*, 1992]. For α between 0.1 and 0.3, we estimate that dehydration could increase V_S by 0.5 to 2%.

[64] We conclude that the combined effects of depletion and dehydration that accompany melt extraction can explain the observed +3% velocity anomaly beneath southwestern Galápagos. By this view, the thickening of the high-velocity lid is consistent with an elevated mantle temperature of at least 1400°C (50°C excess temperature) that depresses the dry solidus and initiates dry melting at depths greater than 70 km (Figure 16).

6. Discussion

6.1. A Plume in the Shallow Upper Mantle

[65] Our results together with receiver function [*Hooft et al.*, 2003] and body wave tomography [*Toomey et al.*, 2002a] studies indicate that the Galápagos hot spot is underlain by a thermal plume that is continuous from the transition zone to the bottom of a high-velocity lid located at depths from 40 to 70 km. Between 120- and 150-km depth the anomalously low velocities are centered near 0.25°S and 91°W, beneath northern Isabela (Figure 12f), and approximately 50 km to the northeast of the center of the deflection of the 410-km discontinuity, which marks the center of hot upwelling through the mantle transition zone [*Hooft et al.*, 2003] (black square in Figure 12f). We interpret the low-velocity anomaly as the locus of an upwelling mantle plume. The lateral extent of the low-velocity anomaly at 130-km depth is approximately 150 km for the -1% $\partial \ln V_S$ contour (Figure 12f).

[66] The low-velocity volume appears to incline northward by approximately 45° from vertical as it shoals between 150- and 100-km depth; the plume conduit is centered at 0.5°S at 150-km depth and at 0° at 100-km depth (Figure 13c). This inclination is also seen in body wave tomography, which detects a low-velocity volume near the southwestern corner of the archipelago that inclines northward as it shoals between 250- and 150-km depth [*Toomey et al.*, 2002a].

[67] As the upwelling mantle plume approaches the high-velocity lid, it begins to flatten and spread in conformance with the shape of the base of the lid. At depths less than ~120 km, the low velocities extend both east and west of 91°W (see -2% $\partial \ln V_S$ contour in Figures 12c–12e and 13b). To the east of 90°W, low velocities are confined to depths shallower than 100 km, a depth that could correspond to the bottom of the spreading plume layer (Figure 13d).

[68] Between 20- and 40-km depth, anomalously low velocities are centered in the southwestern archipelago, above the center of the deflection of the 410-km discontinuity [*Hooft et al.*, 2003] (Figure 12a). One possible interpretation is that this anomaly indicates lithospheric thinning above the center of plume upwelling [*Detrick and Crough*, 1978]. However, the presence of higher-than-normal velocities at depths from 40 to 70 km argues against lithospheric thinning and instead suggests a thicker than normal lid in this region. Our preferred interpretation is that this shallow low-velocity anomaly corresponds to melt accumulation at lithospheric levels. The anomaly lies near Fernandina and Isabela, islands that contain the most active volcanoes in the archipelago, and above the main region of plume upwelling and melt production.

6.2. The High-Velocity Lid

[69] The top of the low-velocity volume appears as a velocity gradient that is present everywhere beneath the archipelago at depths from 40 to 70 km. We suggest that the boundary represents stalling of plume upwelling. As the plume approaches the lid it starts to flatten and spread laterally, conforming to the shape of the lid.

[70] The boundary is deepest beneath the southwestern part of the archipelago and shoals and sharpens toward the east and north. As argued earlier, we suggest that the thick lid observed beneath the southwestern archipelago, above the main region of plume upwelling, corresponds to depleted and dehydrated residuum produced from hot spot melting [e.g., *Phipps Morgan et al.*, 1995; *Ribe and Christensen*, 1999]. To the north and east, the thickness of the lid (~40 km) is less than that expected for residuum (>60 km) created by hot spot melting or ridge melting [e.g., *Evans et al.*, 2005], which could indicate that melting at the GSC produced a weak dehydrated layer. The lid to north and east may thus represent thermal lithosphere.

[71] The variable thickness of the high-velocity lid can be correlated to geochemical and geophysical observations in the Galápagos. The region where the lid is thickest (beneath Isabela and Fernandina) coincides with the region where basalts show higher amounts of enrichment of incompatible elements [e.g., *White et al.*, 1993; *Kurz and Geist*, 1999; *Harpp and White*, 2001] and ^{3}He/^{4}He [*Kurz and Geist*, 1999]. Where the lid is thinner, depleted basalts with decreased contributions of hot spot-related incompatible elements are erupted [*White et al.*, 1993; *Harpp and White*, 2001]. The thin-lid region also coincides approximately with the region of weaker lithosphere inferred from modeling of gravity and bathymetry data [*Feighner and Richards*, 1994].

[72] We suggest that the high-velocity lid has a considerable influence on both plume dynamics and melting beneath the Galápagos region. The variable thickness of the lid controls the final depth of melting and the variability in basalt composition beneath the archipelago. In the eastern archipelago, where depleted basalts erupt, a thinner lid could allow increased amounts of melting from a more depleted source at shallower depths. Conversely, basalts with higher amounts of enrichment erupt in the western

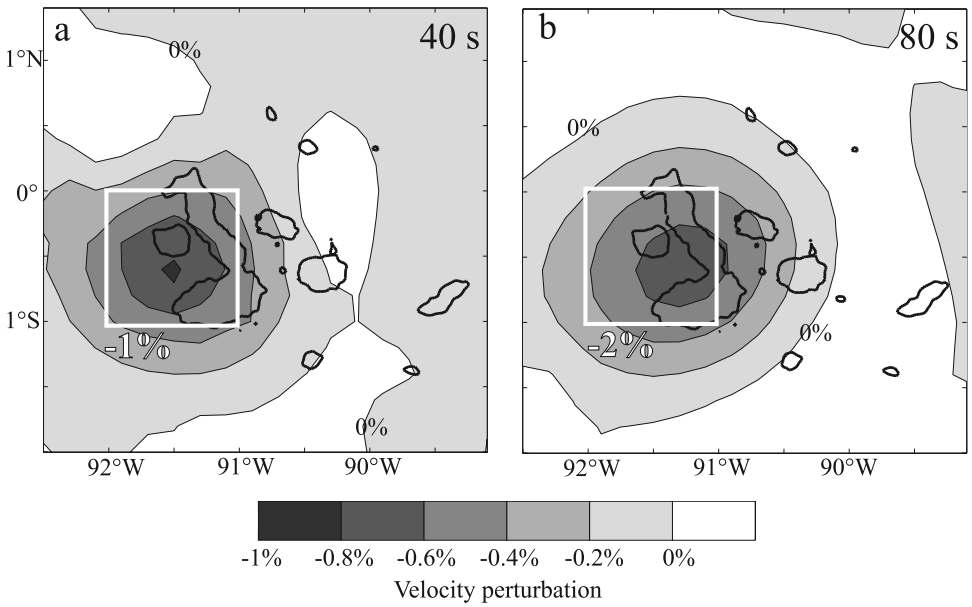

Figure A1. Results of synthetic inversion for phase velocity for period of (a) 40 s and (b) 80 s. White squares indicate synthetic low velocity anomalies of −1 and −2%, respectively. Contours indicate recovered phase velocity anomaly.

archipelago where the lid is thickest. The viscosity increase associated with dehydration [*Hirth and Kohlstedt*, 1996] could decrease plume upwelling and melting above the dry solidus [*Ito et al.*, 1999], and thus a thicker lid could enhance deeper melting of more enriched plume components. Since deep melting is associated with a reduced extent of melting, a relatively high plume flux would be needed to produce the more voluminous volcanism observed in the western archipelago.

6.3. Gravitational Spreading of the Plume

[73] As the upwelling mantle plume approaches the high-velocity lid, it begins to flatten and spread. The low velocities extend mostly eastward at depths shallower than 100 km (Figures 13a and 13b), in the direction of plate motion, suggesting an effect from plate drag. However, the low velocities also appear to extend toward the west of 91.5°W at depths less than 120 km, in a direction opposite to plate motion (Figures 12e, 12e, and 13b). This observation of both eastward and westward plume spreading is consistent with correlated geochemical and geophysical observations along the GSC. Between 83°W and 101°W geochemical and geophysical anomalies are symmetrical about 91.5°W [*Schilling et al.*, 1982, 2003; *Verma and Schilling*, 1982], a longitude that is coincident with the center of plume upwelling beneath the archipelago. We attribute the expansion of the low-velocity volume both to the east and to the west to the gravitational flattening of the plume layer against the variable-thickness lid.

[74] The gravitational spreading of a plume beneath a moving plate represents a balance between buoyancy forces and plate drag forces. This is expressed in the buoyancy number [*Feighner and Richards*, 1995, *Kincaid et al.*, 1995]

$$\Pi_b = Bg/\eta_o U^2, \quad (5)$$

where $B = \Delta\rho Q$ is the buoyancy flux, ρ is density, Q is the volumetric flux, g is gravity, η_o is ambient upper mantle viscosity, and U is plate velocity. The spreading of plume material in a direction opposite to plate motion indicates that plume buoyancy forces dominate over plate drag forces and suggests a high buoyancy flux relative to plate velocity, a low mantle viscosity, or both.

[75] Our observation of upstream flow beneath the Galápagos is consistent with the upper bound of estimates of the Galápagos plume buoyancy flux, which range from B = 1000 kg/s [*Sleep*, 1990] to ∼2000 kg/s [*Schilling*, 1991; *Ribe*, 1996; *Ito et al.*, 1997]. Tank experiments of sheared thermal plumes indicate that upstream plume spreading against plate shear occurs when Π_b is greater than 70–100 [*Kerr and Mériaux*, 2004]. For B = 2000 kg/s, $\eta_o = 4 \times 10^{20}$ Pa s [*Schubert et al.*, 2001], and U = 21 mm/yr (at 0°N, 91°W, for HS3-NUVEL1A) [*Gripp and Gordon*, 2002] the buoyancy number Π_b is 113, within the regime of upstream spreading. A lower estimate of B = 1000 kg/s is probably insufficient to produce upstream flow (Π_b = 56.5). The observation of geophysical and geochemical anomalies up to ∼1000 km east of 91.5°W along the GSC suggest considerable upstream flow and $\Pi_b \gg 100$. Thus B = 2000 kg/s is probably a minimum estimate of plume buoyancy flux.

7. Conclusions

[76] We have imaged with surface waves the three-dimensional shear wave velocity structure of the uppermost mantle beneath the Galápagos Archipelago. From these results we infer the physical state of the mantle and the geometry of mantle flow in the region. We find that the Galápagos hot spot is underlain by a high-velocity lid of variable thickness and a low-velocity asthenosphere consistent with an excess temperature of 30 to 150°C and ∼0.5% melt.

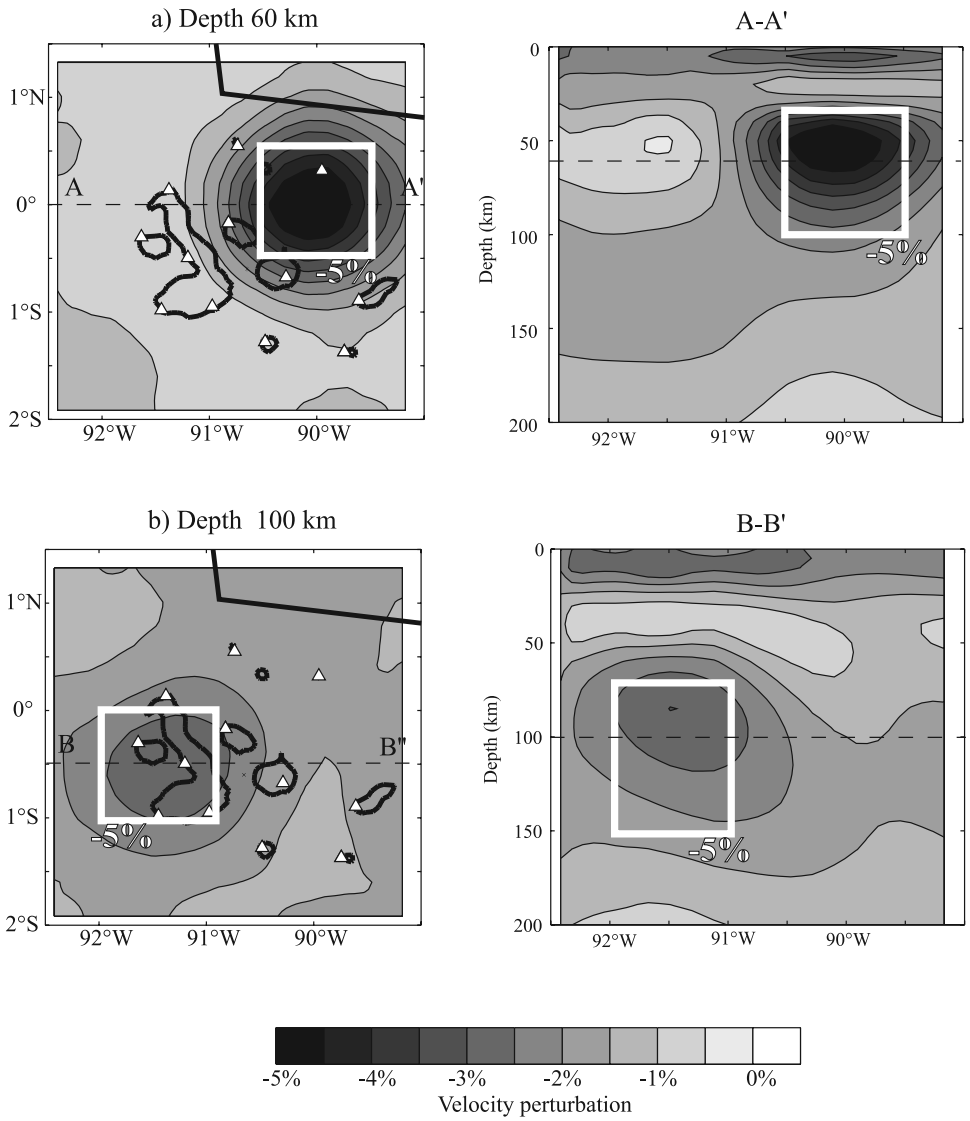

Figure A2. Map views and E-W cross-sections of the results of synthetic inversion for shear wave velocity for a low-velocity anomaly of −5% located in (a) the northeastern archipelago between 40- and 100-km depth and (b) the southwestern archipelago between 70- and 150-km depth. White squares indicate synthetic anomalies. Contours indicate recovered V_S anomaly. White triangles represent seismic stations.

[77] We attribute the thicker-than-normal lid imaged beneath the southwestern archipelago at depths from 40 to 70 km to residuum that is depleted and dehydrated by hot spot melting. The thickness of the high-velocity lid controls the final depth of melting and the spatial variability of basalt composition.

[78] Buoyancy forces appear to dominate over plate drag forces during plume spreading. This finding is indicated by gravitational spreading of plume material in directions both toward and against plate shear at depths less than 120 km. This geometry suggests a relatively high plume buoyancy flux ($B \geq 2000$ kg/s).

Appendix A: Synthetic Inversions and Model Resolution

[79] We here describe a series of inversions of synthetic data carried out to assess the resolution of the models obtained from actual data. We first obtained frequency-dependent two-dimensional phase velocity maps from synthetic models, and then we derived synthetic amplitude and phase data. We included the effect of a complex incoming wavefield in the form of two plane waves with random amplitudes, phases, and deviations from great circle paths. Last, we added random noise to the frequency-dependent phase and amplitude data.

[80] In the first step of the synthetic inversion we inverted the amplitude and phase data for two-dimensional phase velocities and compared them to the synthetic two-dimensional phase velocity maps. In this step we tested the efficacy of the simulated annealing algorithm in recovering the two-plane wave information as well as the horizontal resolution imparted by path coverage and two-dimensional sensitivity kernels. We found that the incoming wavefield was well recovered by correctly estimating the wave parameters for all the primary waves and most of the secondary waves. We

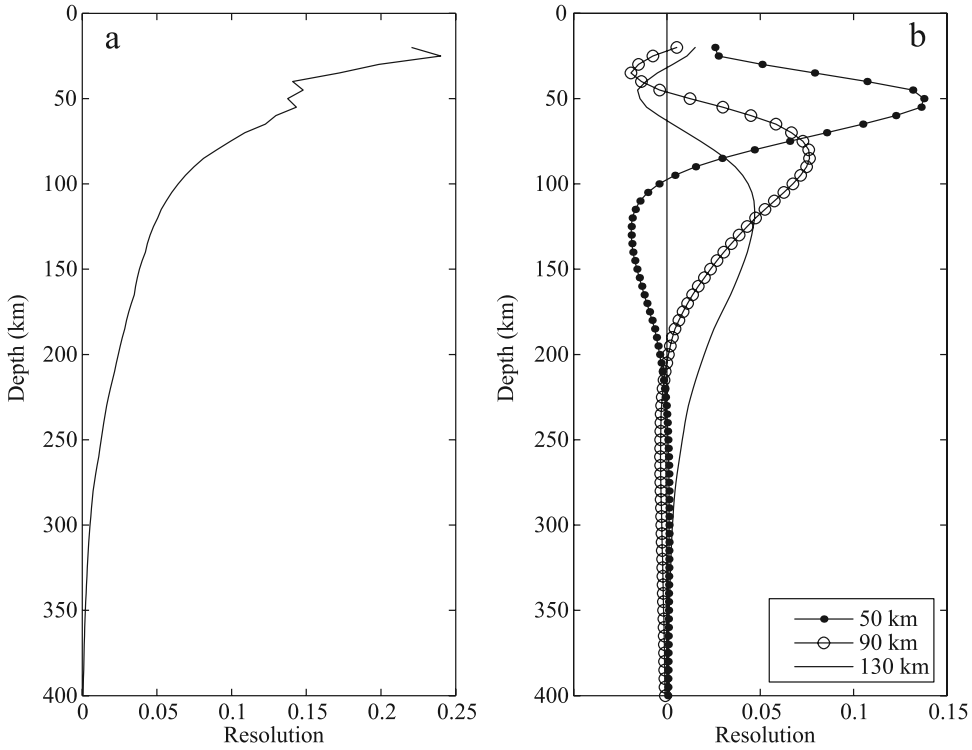

Figure A3. Resolution of V_S inversion for a grid node located at 90.9°W and 0.4°S. (a) Diagonal elements of the resolution matrix as a function of depth. Total rank of the inversion is 3.14. (b) Resolution kernels (rows of resolution matrix) corresponding to depths of 50 (dots), 90 (open circle), and 130 km (solid line) as functions of depth.

also found that, as expected, the horizontal resolution of phase velocity decreases with increasing period. Figure A1 shows example results from the synthetic inversions for two-dimensional phase velocity at periods of 40 and 80 s. The synthetic model, indicated with a white square, has sides of 1° in latitude and longitude, and it represents a phase velocity anomaly of −1% at 40−s period and −2% at 80-s period. The contours indicate the recovered velocity anomalies. The maximum amplitudes of the recovered anomalies are −0.83 and −0.71% for 40 and 80 s, respectively. The path coverage was adequate to recover two-dimensional phase velocity anomalies larger than 100 km in diameter for periods 20−50 s (Figure A1a). For longer-period waves, the recovered velocity anomalies broaden progressively. For example, a 100-km-diameter synthetic phase velocity anomaly appears as a ∼200-km-wide anomaly at 80-s period (Figure A1b). The magnitude of the recovered anomaly also decreases progressively with period. At 80-s period we recovered only ∼30% of the synthetic phase velocity anomaly (Figure A1b), and at 125−s period we recovered only ∼25% of the anomaly.

[81] In a second step we inverted the frequency-dependent phase velocities for three-dimensional V_S structure and compared the solution with the synthetic model. Figure A2 shows examples of synthetic V_S inversions in map view and a vertical E-W cross-section. The synthetic V_S anomalies, indicated with a white rectangle in Figure A2, represent a −5% anomaly. The contours represent the recovered V_S anomalies. Figure A2a shows the result of a synthetic inversion for an anomaly located at depths from 40 to 100 km. The anomaly was fully recovered at depths shallower than 75 km. In addition, the sharp velocity contrast at 40-km depth is well resolved with an uncertainty of 5 to 10 km, while the 5% velocity contrast located at 100-km depth is significantly less well resolved and appears shallower in the synthetic inversions (Figure A2a). Figure A2b shows the synthetic inversion results for an anomaly located from 75- to 150-km depth. We recovered only ∼50% of the anomaly's amplitude between 75- and 110-km depth and 25−40% between 110- and 150-km depth. The depths of the top and bottom of this velocity anomaly are not well resolved and appear shallower in the synthetic inversions.

[82] We find that there is little resolution at depths shallower than 20 km or deeper than 150 km. This effect can also be seen by inspecting the resolution matrix from the inversions of actual data, a direct result of the form of the phase velocity kernels shown in Figure 3c. The trace or rank of the resolution matrix indicates how many parameters were independently resolved. In our inversions we obtained a maximum rank of ∼3, showing that we could resolve only ∼3 independent pieces of information at each grid node. Additionally, the diagonal elements of the resolution matrix indicate how well resolved each velocity parameter is in the inversion (Figure A3a). Resolution is greater at shallower depths, and it rapidly decreases to zero at the bottom of our model. The values of the rows of the resolution matrix at 50-, 90-, and 130-km depth are shown in Figure A3b. These resolution kernels or averaging functions indicate how a model parameter at a given depth depends on information from adjacent layers. Resolution length is a measure of the depth range in the model over which the average velocity is well resolved, i.e., the number

of layers that need to be combined for the rank of that part of the resolution matrix to be equal to 1.0 [*Weeraratne et al.*, 2003]. The resolution length increases with depth in the inversions. For example, at 50-km depth, a 50-km-thick layer is required to recover one independent piece of information about velocity. At 90-km depth, the resolution length is 80 km, and at 130-km depth it increases to 150 km.

[83] Synthetic inversions using alternating positive and negative anomalies indicate that the signs of anomalies with depth extents greater than ~20 km are well recovered between 50- and 150-km depth. In particular, we tested whether the velocity reversal observed beneath the southwestern archipelago at depths between 50 and 75 km (Figures 12b, 12c, and 13a) is an artifact of the inversion, and we found that the sign of such an anomaly can be correctly recovered in synthetic inversions. Some results show artificial velocity reversals at depths shallower than ~50 km (for example, cross-sections A-A′ and B-B′ of Figure A2), mainly because the inversions attempt to compensate for the poor resolution at depths less than 20 km. This effect can be reduced by increasing the amount of damping in the shallowest part of the model during the inversion, as long as the velocities in the upper 15–20 km are well known a priori.

Appendix B: Porous Flow Model

[84] We estimate the volume melt fraction at a depth of 75 km beneath the Galápagos region with a one-dimensional porous flow model in an idealized medium that contains a network of cylindrical tubules that is filled by melt. The pressure gradient that drives the melt upwards is the differential buoyancy of the melt relative to the solid matrix. From Darcy's law, the relative upward velocity between the melt (v_L) and the solid (v_S) is

$$v_L - v_S = -\frac{b^2\phi(\rho_S - \rho_L)}{24\pi\mu}, \tag{B1}$$

where b is grain size, ϕ is the melt porosity, ρ_L is the melt density, ρ_S is the density of the solid, and μ is the melt viscosity. The melt fraction flux F is defined as the ratio of the total upward mass flux of melt to the upward mass flux of rock prior to the onset of melting, or [*Turcotte and Schubert*, 2002]

$$F \equiv \frac{\phi\rho_L(v_L + 2v_S)/3}{\rho_S v_0}, \tag{B2}$$

where v_0 is the upward velocity of rock prior to melting. Combining equations (B1) and (B2) with the equation for conservation of mass, and assuming $\phi \ll 1$, we obtain [*Turcotte and Schubert*, 2002]

$$v_S = v_0(1 - F), \text{ and} \tag{B3}$$

$$v_L = -\frac{|v_S|}{2} + \left\{\frac{9v_S^2}{4} + \frac{F\rho_S g(\rho_S - \rho_L)b^2|v_0|}{8\pi\mu\rho_L}\right\}^{1/2}. \tag{B4}$$

[85] The melt porosity ϕ can be found by solving equation (B1). We use the parameters ρ_L = 2700 kg/m^3, ρ_S = 3300 kg/m^3, μ = 10 Pa s, and v_0 = 100 mm/y. We estimate the melt fraction flux F by assuming that it is equivalent to the extent of melting (for example, F in *Langmuir et al.* [1992]). Melt productivity $\partial F/\partial P$ is ~1%/GPa for water-induced melting at temperatures below the dry solidus [*Asimow et al.*, 2004] and between 12 and 20%/GPa in the dry melting regime [*Langmuir et al.*, 1992]. We adopt constant melt productivity values of $\partial F/\partial P$ = 1%/GPa below the dry solidus and $\partial F/\partial P$ = 15%/GPa above the dry solidus. We use the analytical dry solidus of *McKenzie and Bickle* [1988] to determine the depth to the solidus as a function of potential temperature. Thus ϕ is a function of both mantle potential temperature and grain size b. We estimate melt fraction to be ~0.05–0.5% at 75-km depth for grain sizes from 1 to 10 mm and mantle potential temperatures from 1300° to 1600°C.

[86] **Acknowledgments.** We thank Don Forsyth, Garrett Ito, and Michael Ritzwoller for comments and suggestions that substantially improved this paper. We also thank Don Forsyth, Dayanthie Weeraratne, Yingjie Yang, and Uli Faul for providing computer code and for useful suggestions. We also thank Dennis Geist, Karen Harpp, Mark Jellinek, Derek Schutt, and Alexander McBirney for discussions. We are particularly grateful to Minard Hall of the Instituto Geofisico of the Escuela Politécnica Nacional in Quito, the Charles Darwin Research Station, and the Parque Nacional Galápagos for logistical support and assistance in the field. This research was supported by the National Science Foundation under grants OCE-9908695 and OCE-0221549 to the University of Oregon and OCE-0221634 to the Carnegie Institution of Washington.

References

Allen, R. M., et al. (2002), Imaging the mantle beneath Iceland using integrated seismological techniques, *J. Geophys. Res.*, *107*(B12), 2325, doi:10.1029/2001JB000595.

Asimow, P. D., and C. H. Langmuir (2003), The importance of water to oceanic mantle melting regimes, *Nature*, *421*, 815–820.

Asimow, P. D., J. E. Dixon, and C. H. Langmuir (2004), A hydrous melting and fractionation model for mid-ocean ridge basalts: Application to the Mid-Atlantic Ridge near the Azores, *Geochem. Geophys. Geosyst.*, *5*, Q01E16, doi:10.1029/2003GC000568.

Christensen, N. I. (1984), The magnitude, symmetry and origin of upper mantle anisotropy based on fabric analyses of ultramafic tectonites, *Geophys. J. R. Astron. Soc.*, *76*, 89–111.

DeMets, C., R. G. Gordon, D. F. Argus, and S. Stein (1994), Effect of recent revisions to the geomagnetic reversal time scale on estimates of current plate motions, *Geophys. Res. Lett.*, *21*, 2191–2194.

Detrick, R. S., and S. T. Crough (1978), Island subsidence, hot spots, and lithospheric thinning, *J. Geophys. Res.*, *83*, 1236–1244.

Detrick, R. S., J. M. Sinton, G. Ito, J. P. Canales, M. Behn, T. Blacic, B. Cushman, J. E. Dixon, D. W. Graham, and J. J. Mahoney (2002), Correlated geophysical, geochemical, and volcanological manifestations of plume-ridge interaction along the Galápagos Spreading Center, *Geochem. Geophys. Geosyst.*, *3*(10), 8501, doi:10.1029/2002GC000350.

Ding, X., and S. P. Grand (1993), Upper mantle Q structure beneath the East Pacific Rise, *J. Geophys. Res.*, *98*, 1973–1985.

Dziewonski, A. M., and D. L. Anderson (1981), Preliminary reference Earth model, *Phys. Earth Planet Inter.*, *25*, 297–356.

Evans, R. L., G. Hirth, K. Baba, D. Forsyth, A. Chave, and R. Mackie (2005), Geophysical evidence from the MELT area for compositional controls on oceanic plates, *Nature*, *437*, 249–252.

Faul, U. H. (2001), Melt retention and segregation beneath mid-ocean ridges, *Nature*, *410*, 920–923.

Faul, U. H., and I. Jackson (2005), The seismological signature of temperature and grain size variations in the upper mantle, *Earth Planet. Sci. Lett.*, *234*, 119–134.

Feighner, M. A., and M. A. Richards (1994), Lithospheric structure and compensation mechanisms of the Galápagos archipelago, *J. Geophys. Res.*, *99*, 6711–6729.

Feighner, M. A., and M. A. Richards (1995), The fluid dynamics of plume-ridge and plume-plate interactions: An experimental investigation, *Earth Planet. Sci. Lett.*, *129*, 171–182.

Fontaine, F. R., E. E. E. Hooft, P. G. Burkett, D. R. Toomey, S. C. Solomon, and P. G. Silver (2005), Shear-wave splitting beneath the Galápagos archipelago, *Geophys. Res. Lett.*, *32*, L21308, doi:10.1029/2005GL024014.

Forsyth, D. W., and A. Li (2005), Array analysis of two-dimensional variations in surface wave phase velocity and azimuthal anisotropy in the

presence of multipathing interference, in *Seismic Earth: Array Analysis of Broadband Seismograms*, edited by A. Levander and G. Nolet, Geophysical Monograph 157, pp. 81–97, AGU, Washington, D.C.

Forsyth, D. W., S. C. Webb, L. M. Dorman, and Y. Shen (1998), Phase velocities of Rayleigh waves in the MELT experiment on the East Pacific Rise, *Science*, *280*, 1235–1238.

Geist, D. J., W. M. White, and A. R. McBirney (1988), Plume-asthenosphere mixing beneath the Galapagos archipelago, *Nature*, *333*, 657–660.

Granet, M., M. Wilson, and U. Achauer (1995), Imaging a mantle plume beneath the French Massif Central, *Earth Planet. Sci. Lett.*, *136*, 281–296.

Gripp, A. E., and R. G. Gordon (2002), Young tracks of hotspots and current plate velocities, *Geophys. J. Int.*, *150*, 321–361.

Gu, Y. J., S. C. Webb, A. Lerner-Lam, and J. B. Gaherty (2005), Upper mantle structure beneath the eastern Pacific Ocean ridges, *J. Geophys. Res.*, *110*, B06305, doi:10.1029/2004JB003381.

Hammond, W. C., and E. D. Humphreys (2000), Upper mantle seismic wave velocity: Effects of realistic partial melt geometries, *J. Geophys. Res.*, *105*, 10,975–10,986.

Harpp, K. S., and W. M. White (2001), Tracing a mantle plume: Isotopic and trace element variations of Galapagos seamounts, *Geochem. Geophys. Geosyst.*, *2*(6), doi:10.1029/2000GC000137.

Hirth, G., and D. L. Kohlstedt (1996), Water in the oceanic upper mantle: Implications for rheology, melt extraction and the evolution of the lithosphere, *Earth Planet. Sci. Lett.*, *144*, 93–108.

Hirth, G., and D. L. Kohlstedt (2003), Rheology of the upper mantle and the mantle wedge: A view from experimentalists, in *Inside the Subduction Factory*, edited by J. M. Eiler, Geophysical Monograph 138, pp. 83–105, AGU, Washington, D.C.

Hooft, E. E. E., D. R. Toomey, and S. C. Solomon (2003), Anomalously thin transition zone beneath the Galápagos hotspot, *Earth Planet. Sci. Lett.*, *216*, 55–64.

Ito, G., J. Lin, and C. W. Gable (1997), Interaction of mantle plumes and migrating mid-ocean ridges: Implications for the Galapagos plume-ridge system, *J. Geophys. Res.*, *102*, 15,403–15,417.

Ito, G., Y. Shen, G. Hirth, and C. J. Wolfe (1999), Mantle flow, melting, and dehydration of the Iceland mantle plume, *Earth Planet. Sci. Lett.*, *165*, 81–96.

Ito, G., J. Lin, and D. Graham (2003), Observational and theoretical studies of the dynamics of mantle plume-mid-ocean ridge interaction, *Rev. Geophys.*, *41*(4), 1017, doi:10.1029/2002RG000117.

Jackson, I., M. S. Paterson, and J. D. FitzGerald (1992), Seismic wave dispersion and attenuation in Aheim dunite, *Geophys. J. Int.*, *108*, 517–534.

Karato, S. (1986), Does partial melting reduce the creep strength of the upper mantle?, *Nature*, *319*, 309–310.

Karato, S. (1993), Importance of anelasticity in the interpretation of seismic tomography, *Geophys. Res. Lett.*, *20*, 1623–1626.

Karato, S. (2003), Mapping water content in the upper mantle, in *Inside the Subduction factory,* edited by J. M. Eiler, Geophysical Monograph 138, pp. 135–152, AGU, Washington, D.C.

Karato, S., and H. Jung (1998), Water, partial melt and the origin of the seismic low velocity and high attenuation zone in the upper mantle, *Earth Planet. Sci. Lett.*, *157*, 193–207.

Kerr, R. C., and C. Mériaux (2004), Structure and dynamics of sheared mantle plumes, *Geochem. Geophys. Geosyst.*, *5*, Q12009, doi:10.1029/2004GC000749.

Kincaid, C., G. Ito, and C. Gable (1995), Laboratory investigation of the interaction of off-axis mantle plumes and spreading centers, *Nature*, *376*, 758–761.

Kurz, M. D., and D. Geist (1999), Dynamics of the Galapagos hotspot from helium isotope geochemistry, *Geochim. Cosmochim. Acta*, *63*, 4139–4156.

Langmuir, C. H., E. M. Klein, and T. Plank (1992), Petrological systematics of mid-ocean ridge basalts: Constraints on melt generation beneath ocean ridges, in *Mantle Flow and Melt Generation at Mid-Ocean Ridges*, edited by J. Phipps Morgan, D. K. Blackman, and J. M. Sinton, Geophysical Monograph 71, pp. 183–280, AGU, Washington, D.C.

Larson, E. W. F., and G. Ekström (2002), Determining surface wave arrival angle anomalies, *J. Geophys. Res.*, *107*(B6), 2127, doi:10.1029/2000JB000048.

Li, A., and R. S. Detrick (2006), Seismic structure of Iceland from Rayleigh wave inversions and geodynamic implications, *Earth Planet. Sci. Lett.*, *241*, 901–912.

Li, A., D. W. Forsyth, and K. M. Fischer (2003), Shear velocity structure and azimuthal anisotropy beneath eastern North America from Rayleigh wave inversion, *J. Geophys. Res.*, *108*(B8), 2362, doi:10.1029/2002JB002259.

Lundstrom, C. C., J. Gill, Q. Williams, and M. R. Perfit (1995), Mantle melting and basalt extraction by equilibrium porous flow, *Science*, *270*, 1958–1961.

Matsukage, K. N., Y. Nishihara, and S. Karato (2005), Seismological signature of chemical differentiation of Earth's upper mantle, *J. Geophys. Res.*, *110*, B12305, doi:10.1029/2004JB003504.

McBirney, A. R., and H. Williams (1969), *Geology and Petrology of the Galapagos Islands*, Memoir 118, 197 pp., Geol. Soc. of Am., Boulder, Colo.

McKenzie, D., and M. J. Bickle (1988), The volume and composition of melt generated by extension of the lithosphere, *J. Petrol.*, *29*, 625–679.

Montagner, J. P., and T. Tanimoto (1990), Global anisotropy in the upper mantle inferred from the regionalization of phase velocities, *J. Geophys. Res.*, *95*, 4797–4819.

Morgan, W. J. (1971), Convection plumes in the lower mantle, *Nature*, *230*, 42–43.

Nishimura, C. E., and D. W. Forsyth (1988), Rayleigh wave phase velocities in the Pacific with implications for azimuthal anisotropy and lateral heterogeneities, *Geophys. J.*, *94*, 479–501.

Nishimura, C. E., and D. W. Forsyth (1989), The anisotropic structure of the upper mantle in the Pacific, *Geophys. J. R. Astron. Soc.*, *96*, 203–229.

Phipps Morgan, J., W. J. Morgan, and E. Price (1995), Hotspot melting generates both hotspot volcanism and a hotspot swell?, *J. Geophys. Res.*, *100*, 8045–8062.

Press, W. H., S. A. Teukolsky, W. T. Vetterling, and B. P. Flannery (1992), *Numerical Recipes in FORTAN: The Art of Scientific Computing*, 2nd ed., 963 pp., Cambridge Univ. Press, New York.

Priestley, K., and F. Tilmann (1999), Shear-wave structure of the lithosphere above the Hawaiian hot spot from two-station Rayleigh wave phase velocity measurements, *Geophys. Res. Lett.*, *26*, 1493–1496.

Ribe, N. M. (1996), The dynamics of plume-ridge interaction: 2. Off-ridge plumes, *J. Geophys. Res.*, *101*, 16,195–16,204.

Ribe, N. M., and U. R. Christensen (1994), Three-dimensional modeling of plume-lithosphere interaction, *J. Geophys. Res.*, *99*, 669–682.

Ribe, N. M., and U. R. Christensen (1999), The dynamical origin of Hawaiian volcanism, *Earth Planet. Sci. Lett.*, *171*, 517–531.

Ribe, N. M., and W. L. Delattre (1998), The dynamics of plume-ridge interaction: III. The effects of ridge migration, *Geophys. J. Int.*, *133*, 511–518.

Richards, M. A., and R. W. Griffiths (1989), Thermal entrainment by deflected mantle plumes, *Nature*, *342*, 900–902.

Ritter, J. R. R., M. Jordan, U. R. Christensen, and U. Achauer (2001), A mantle plume below the Eifel volcanic fields, Germany, *Earth Planet. Sci. Lett.*, *186*, 7–14.

Saito, M. (1988), DISPER80: A subroutine package for calculation of seismic normal-mode solutions, in *Seismological Algorithms; Computational Methods and Computer Programs*, edited by D. J. Doornbos, pp. 293–319, Elsevier, New York.

Schilling, J. G. (1991), Fluxes and excess temperatures of mantle plumes inferred from their interaction with migrating mid-ocean ridges, *Nature*, *352*, 397–403.

Schilling, J. G., R. H. Kingsley, and J. D. Devine (1982), Galapagos hot spot-spreading center system: 1. Spatial petrological and geochemical variations (83°W–101°W), *J. Geophys. Res.*, *87*, 5593–5610.

Schilling, J. G., D. Fontignie, J. Blichert-Toft, R. Kingsley, and U. Tomza (2003), Pb-Hf-Nd-Sr isotope variations along the Galápagos Spreading Center (101°–83°W): Constraints on the dispersal of the Galápagos mantle plume, *Geochem. Geophys. Geosyst.*, *4*(10), 8512, doi:10.1029/2002GC000495.

Schubert, G., D. L. Turcotte, and P. Olson (2001), *Mantle Convection in the Earth and Planets*, 940 pp., Cambridge Univ. Press, New York.

Simkin, T., and L. Siebert (1994), *Volcanoes of the World; A Regional Directory, Gazetteer, and Chronology of Volcanism during the Last 10,000 Years*, 349 pp., Geoscience Press, Tucson, Ariz.

Sinton, C. W., D. M. Christie, and R. A. Duncan (1996), Geochronology of Galápagos seamounts, *J. Geophys. Res.*, *101*, 13,689–13,700.

Sleep, N. H. (1990), Hotspots and mantle plumes: Some phenomenology, *J. Geophys. Res.*, *95*, 6715–6736.

Sleep, N. H. (1996), Lateral flow of hot plume material ponded at sublithospheric depths, *J. Geophys. Res.*, *101*, 28,065–28,083.

Smith, M. L., and F. A. Dahlen (1973), The azimuthal dependence of Love and Rayleigh wave propagation in a slightly anisotropic medium, *J. Geophys. Res.*, *78*, 3321–3333.

Tarantola, A., and B. Valette (1982), Generalized nonlinear inverse problems solved using the least squares criterion, *Rev. Geophys.*, *20*, 219–232.

Tilmann, F. J. (1999), The seismic structure of the upper mantle beneath Hawaii, Ph.D. thesis, Queens' College, Cambridge.

Toomey, D. R., E. E. E. Hooft, and R. S. Detrick (2001), Crustal thickness variations and internal structure of the Galápagos Archipelago, *Eos Trans. AGU*, *82*(47), Fall Meeting Suppl., Abstract T42B-0939.

Toomey, D. R., E. E. E. Hooft Toomey, S. C. Solomon, D. E. James, and M. L. Hall (2002a), Seismic evidence for a plume beneath the Galápagos hotspot, *Eos Trans. AGU*, *83*(47), Fall Meet. Suppl., Abstract S72C-02.

Toomey, D. R., W. S. D. Wilcock, J. A. Conder, D. W. Forsyth, J. D. Blundy, E. M. Parmentier, and W. C. Hammond (2002b), Asymmetric mantle dynamics in the MELT region of the East Pacific Rise, *Earth Planet. Sci. Lett.*, *200*, 287–295.

Turcotte, D. L., and G. Schubert (2002), *Geodynamics*, 2nd ed., 456 pp., Cambridge Univ. Press, New York.

Verma, S. P., and J.-G. Schilling (1982), Galapagos hot spot-spreading center system: 2. $^{87}Sr/^{86}Sr$ and large ion lithophile element variations (85°W-101°W), *J. Geophys. Res.*, *87*, 10,838–10,856.

Vidale, J. E. (1986), Complex polarization analysis of particle motion, *Bull. Seismol. Soc. Am.*, *76*, 1393–1405.

Weeraratne, D. S., D. W. Forsyth, K. M. Fischer, and A. A. Nyblade (2003), Evidence for an upper mantle plume beneath the Tanzanian craton from Rayleigh wave tomography, *J. Geophys. Res.*, *108*(B9), 2427, doi:10.1029/2002JB002273.

White, W. M., and A. W. Hofmann (1978), Geochemistry of the Galapagos Islands: Implications for mantle dynamics and evolution, in *Year Book 77*, pp. 596–606, Carnegie Institution of Washington, Washington, D.C.

White, R. S., and D. McKenzie (1995), Mantle plumes and flood basalts, *J. Geophys. Res.*, *100*, 17,543–17,586.

White, R. S., D. McKenzie, and R. K. O'Nions (1992), Oceanic crustal thickness from seismic measurements and rare earth element inversions, *J. Geophys. Res.*, *97*, 19,683–19,715.

White, W. M., A. R. McBirney, and R. A. Duncan (1993), Petrology and geochemistry of the Galapagos Islands: Portrait of a pathological mantle plume, *J. Geophys. Res.*, *98*, 19,533–19,563.

Wilson, D. S., and R. N. Hey (1995), History of rift propagation and magnetization intensity for the Cocos-Nazca spreading center, *J. Geophys. Res.*, *100*, 10,041–10,056.

Wolfe, C. J., and S. C. Solomon (1998), Shear-wave splitting and implications for mantle flow beneath the MELT region of the East Pacific Rise, *Science*, *280*, 1230–1232.

Wolfe, C. J., I. T. Bjarnason, J. C. VanDecar, and S. C. Solomon (1997), Seismic structure of the Iceland mantle plume, *Nature*, *385*, 245–247.

Yale, M. M., and J. Phipps Morgan (1998), Asthenosphere flow model of hotspot-ridge interactions: A comparison of Iceland and Kerguelen, *Earth Planet. Sci. Lett.*, *161*, 45–56.

Yang, Y., and D. W. Forsyth (2006), Regional tomographic inversion of the amplitude and phase of Rayleigh waves with two-dimensional sensitivity kernels, *Geophys. J. Int.*, *166*, 1148–1160.

Zhou, Y., F. A. Dahlen, and G. Nolet (2004), Three-dimensional sensitivity kernels for surface wave observables, *Geophys. J. Int.*, *158*, 142–168.

E. E. E. Hooft, D. R. Toomey, and D. R. Villagómez, Department of Geological Sciences, University of Oregon, Eugene, Oregon, USA. (darwin7@gmail.com)

S. C. Solomon, Department of Terrestrial Magnetism, Carnegie Institution of Washington, Washington, D. C., USA.